Engineering Structures 272 (2022) 114972

Contents lists available at ScienceDirect

Engineering Structures

journal homepage: www.elsevier.com/locate/engstruct

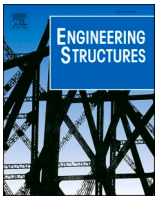

Flexural behaviour of concrete-filled double skin aluminium alloy tubes

Shafayat Bin Ali [a,b,*], George S. Kamaris [a], Michaela Gkantou [a]

[a] School of Civil Engineering and Built Environment, Liverpool John Moores University, Liverpool L3 3AF, United Kingdom
[b] Institute of Earthquake Engineering Research, Chittagong University of Engineering & Technology, Chattogram 4349, Bangladesh

ARTICLE INFO

Keywords:
6082-T6 aluminium alloy
Flexural members
Concrete-filled double skin tubes
Flexural behaviour
Experiments
Finite Element modelling
Design

ABSTRACT

Concrete-filled double skin structural members, comprising of two metal tubes and concrete infill between them, have been gaining popularity in structural engineering because of their high strength, large stiffness, good ductility and easy maintenance. The use of aluminium tubes in these members can further enhance their performance, as aluminium alloy offers lightweight and good corrosion resistance. This study presents experimental and numerical investigations on the flexural behaviour of concrete-filled double skin aluminium alloy tubular (CFDSAT) members under in-plane bending. A total of 10 CFDSAT beams, including 3 specimens with square outer and inner tubes, 2 specimens with square outer and circular inner tubes and 5 specimens with circular outer and inner tubes, were tested. The failure modes, flexural strength and bending moment versus mid-span deflection curves obtained from the experiments are reported. Finite element (FE) models of the CFDSAT beams were developed and validated against the experimental results. The validated FE models were adopted to carry out a parametric study to examine the influence of cross-section slenderness of inner and outer tubes, hollow ratio, concrete compressive strength, cross-section shape and composite action on the flexural behaviour of CFDSAT beams. In the absence of design rules for CFDSAT beams, a design methodology, which is based on the Eurocode 4 framework, is proposed to determine the flexural strength of square and circular CFDSAT members. Moreover, slenderness limits for square and circular CFDSAT cross-sections are proposed based on the data obtained from the experiments and FE analyses.

1. Introduction

Concrete-filled double skin tubes have been gaining popularity in structural engineering owing to their high strength, large stiffness, good ductility and easy maintenance. This new type of structural member is usually made with two steel tubes and concrete infill between them. The main advantage of concrete-filled double skin steel tubular (CFDSST) cross-sections over the concrete-filled steel tubular (CFST) ones is the lower self-weight, which is achieved by the replacement of the inner concrete core with a hollow steel tube [1]. Thus, this type of concrete-filled section is more efficient and can provide better seismic performance to structural systems. It can also be cost-effective as the cost of a structure can be significantly reduced due to savings in material and labour costs. Moreover, CFDSST members have better local and global stability because of the interaction of three components [2] and improved fire resistance owing to the concrete infill and inner tube being thermally protected by the outer tube [3]. Aluminium alloy is a promising material in the construction industry because of its light weight and good corrosion resistance [4–6]. Thus, aluminium alloys can be used for the outer and inner profiles of concrete-filled double skin tubular structural members to improve their sustainability and resilience. In addition, past research showed that the composite action of aluminium alloys and concrete can improve aluminium's stability performance [7–11].

Extensive research studies have been carried out on the behaviour of CFDSST structural members fabricated by different steel materials under different loading conditions. A series of experiments were conducted on CFDSST short columns consisting of carbon steel square [12], rectangular [13], circular [14–16], circular-square [17] and square-circular [18] outer and inner sections, respectively. In these studies, the failure mechanism and compressive strength of CFDSST members were investigated and design formulae were proposed to determine their capacity. Experimental investigations were conducted on the compressive response of CFDSST stub columns manufactured by stainless outer and carbon inner tubes with square, rectangular sections [19], circular sections [20], square outer and circular inner sections [21] and round-up rectangular and elliptical sections [22]. Based on the results of these studies, design recommendations were suggested for these columns. The structural response of CFDSST stub columns subjected to large

* Corresponding author at: School of Civil Engineering and Built Environment, Liverpool John Moores University, Liverpool L3 3AF, United Kingdom.
E-mail addresses: S.B.Ali@2019.ljmu.ac.uk, shafayat@cuet.ac.bd (S. Bin Ali).

https://doi.org/10.1016/j.engstruct.2022.114972
Received 12 April 2022; Received in revised form 31 August 2022; Accepted 12 September 2022
Available online 22 September 2022

Nomenclature

A_c	area of concrete
B_o	width of outer tube
B_i	width of inner tube
D_o	depth/diameter of outer tube
D_i	depth/diameter of inner tube
E	modulus of Elasticity
f	tensile stress
f_c	concrete cylinder compressive strength
f_{cu}	concrete cube compressive strength
f_u	ultimate tensile stress
$f_{0.1}$	0.1 % proof stress
$f_{0.2}$	0.2 % proof stress
h_n	distance between plastic neutral axis and centre line of cross-section
L	distance between two supports
L_l	distance between two loading points
M_{pl}	plastic moment capacity
M_u	flexural strength
$M_{u,FE}$	flexural strength obtained from FE analysis
$M_{u,prop}$	design flexural strength
$M_{u,Test}$	flexural strength obtained from test
n	strain hardening exponent
P	applied load
t_o	thickness of outer tube
t_i	thickness of inner tube
W_{pla_i}	plastic modulus of inner tube
W_{pla_o}	plastic modulus of outer tube
W_{plc}	plastic modulus of concrete
$W_{pla_i,n}$	plastic modulus of inner tube at $2h_n$
$W_{pla_o,n}$	plastic modulus of outer tube at $2h_n$
$W_{plc,n}$	plastic modulus of concrete at $2h_n$
α	hollow ratio
β	ratio of outer width to outer thickness
δ	mid-span displacement at ultimate moment
δ_{av}	average vertical displacement of two loading points at ultimate moment
ε	material factor
ε_f	strain at fracture
ε_u	strain at ultimate stress
κ	curvature of beam

deformation under compressive loading [23], long-term sustained load [24] and cyclic load [25] was also studied. Hassanein and Kharoob [26], Sulthana and Jayachandran [27], Zhao et al. [28] and Ahmed et al. [29] investigated the behaviour of CFDSST slender columns made with different cross-sectional configurations and steel materials and suggested design equations to predict the strength of these columns. Experimental studies were carried out on CFDSST beams with different profiles: circular profiles were used by Uenaka et al. [30], Xiong et al. [31], Eom et al. [32] and Viet et al. [33]; square profiles by Zhao and Grzebieta [12]; rectangular profiles by Tao and Han [13]; dodecagonal profile by Chen et al. [34]; and square outer and circular inner profiles by Han et al. [18]. In these studies, the effect of cross-section dimensions of outer and inner tubes on the bending performance of CFDSST members was investigated and design methodologies were provided to estimate their flexural capacity. Wang et al. [1] and Zhao et al. [28] experimentally and numerically studied the response of circular CFDSST beams made of stainless-steel outer tubes. Based on their results they assessed the applicability of current design rules available for CFST beams for the design of CFDSST flexural members.

Few research studies are available on the structural response of concrete-filled double skin aluminium alloy tubular (CFDSAT) members. Zhou and Young [35,36] carried out experimental and numerical research to examine the effect of geometric dimensions and concrete compressive strength on the compressive response of 6061-T6 alloy CFDSAT stub columns consisting of circular tubes and a combination of circular outer and square inner tubes. They proposed design equations for CFDSAT stub columns considering the composite response of aluminium tubes and concrete. Patel et al. [37] proposed a fibre model to investigate the response of concentrically compressed circular CFDSAT short columns and suggested an expression to determine the lateral confining pressure of concrete infill.

1.1. Research significance

Up-to-date concrete-filled double skin cross-sections have been applied mainly for the structural members in compression. However, in most applications in practice, compression structural members are subjected to a combination of axial compression force and bending moment, where the flexure develops because of unavoidable eccentricities of axial force, frame action, second order effects and transverse loads, such as seismic and wind loads. For the design of such structural members subjected to combined loading, bending moment versus axial load interaction curves are required, which are constructed by knowing the resistance of the members against pure and eccentric compression and pure bending. The literature review presented in the previous section shows that research on CFDSAT members is very limited and there is no research on the flexural response of CFDSAT members. To design these structural members and facilitate their practical application, it is essential to have knowledge of their structural response under pure bending. Hence, in this study, the behaviour of CFDSAT members under in-plane bending is experimentally and numerically investigated for the first time. The aluminium hollow tubes used in this study were fabricated by 6082-T6 alloy, a material gaining a lot of attention in the modern construction sector [7,38] due to its high strength, better corrosion resistance and good weldability. The generated test and numerical data will contribute to the literature by adding information related to the structural response of CFDSAT flexural members as the behaviour of these members is still unexplored. Moreover, due to the absence of design rules, this study proposes a design methodology for CFDSAT flexural members based on the framework of Eurocode 4 (EC4) [39]. Overall, the findings of this research show the potential of CFDSAT flexural members for structural applications in aggressive environments, seismic-prone areas and offshore industry, as they combine the sustainability of aluminium alloys with the effectiveness of double skin technique.

2. Experimental investigation

2.1. Concrete-filled double skin specimens

A total of 10 CFDSAT members, including 3 specimens with square outer and inner tubes, 2 specimens with square outer and circular inner tubes and 5 specimens with circular outer and inner tubes, were tested under in-plane bending. 6082-T6 aluminium alloy was used for the inner and outer hollow tubes, which were fabricated by the extrusion process. However, only two inner tubes, i.e., S19.2 × 1.6 and C88.6 × 1.6 were manufactured using 6063-T6 aluminium alloy. The measured geometric dimensions of all specimens are reported in Table 1 and the geometry of typical cross-sections of the specimens are presented in Fig. 1, in which D_o, B_o and t_o are the depth/diameter, width and thickness of outer tube,

Table 1
Measured geometric dimensions of CFDSAT specimens.

Specimen	D_o (mm)	B_o (mm)	t_o (mm)	D_o/t_o	D_i (mm)	B_i (mm)	t_i (mm)	D_i/t_i
S76.2 × 6.4-S19.2 × 1.6	76.24	76.30	6.31	12.08	19.07	19.07	1.60	11.92
S76.2 × 6.4-S25.4 × 3.2	76.23	76.30	6.26	12.18	25.39	25.39	3.24	7.84
S76.2 × 4.8-S25.4 × 3.2	76.10	76.30	4.57	16.65	25.39	25.39	3.24	7.84
S76.2 × 6.4-C25.4 × 3.2	76.17	76.30	6.22	12.25	25.41	–	3.36	7.56
S76.2 × 6.4-C38.2 × 1.6	76.20	76.30	6.29	12.11	38.03	–	1.64	23.19
C88.6 × 1.6-C19.2 × 3.2	88.69	–	1.55	57.22	18.86	–	3.12	6.04
C88.6 × 1.6-C25.4 × 3.2	88.66	–	1.60	55.41	25.41	–	3.39	7.50
C88.6 × 1.6-C38.2 × 1.6	88.61	–	1.50	59.07	38.03	–	1.57	24.22
C76.2 × 3.2-C25.4 × 3.2	76.15	–	3.22	23.65	25.36	–	3.34	7.59
C76.2 × 3.2-C38.2 × 1.6	76.19	–	3.31	23.02	38.00	–	1.59	23.90

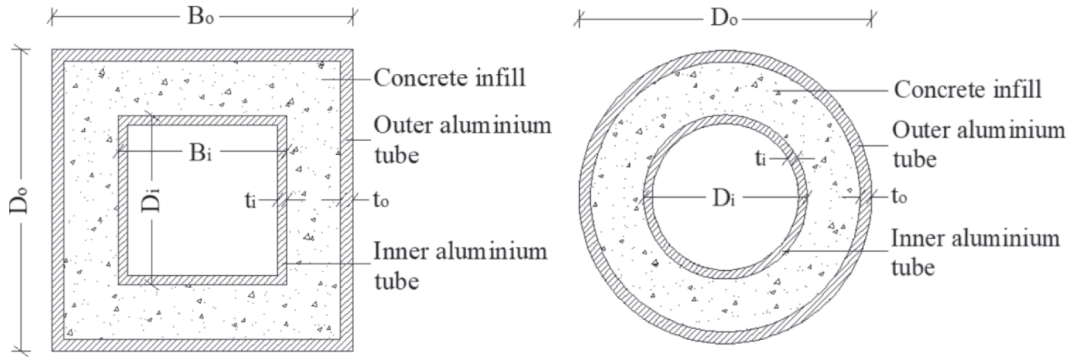

(a) Square CFDSAT specimen (b) Circular CFDSAT specimen

Fig. 1. Geometry of typical cross-sections of CFDSAT specimens.

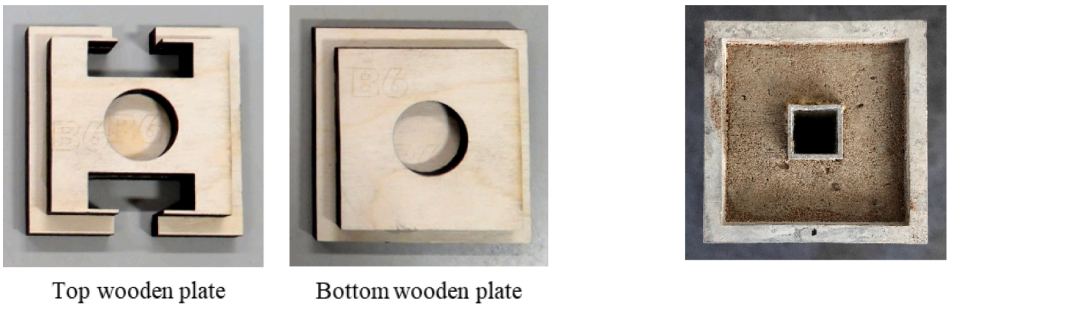

(a) Wooden plates

(b) CFDSAT specimen with square outer and inner tubes

(c) CFDSAT specimen with square outer and circular inner tubes

(d) CFDSAT specimen with circular outer and inner tubes

Fig. 2. Photographs of wooden plates and typical cross-sections of CFDSAT specimens.

respectively and D_i, B_i and t_i are the depth/diameter, width and thickness of inner tube, respectively. The hollow tubes consisted of eight different cross-sections, of which four large sections were used for outer tube with measured depth/diameter to thickness ratio (D_o/t_o) ranging from 12.08 to 59.07 and four small sections were used for inner tube with measured depth/diameter to thickness ratio (D_i/t_i) varied from 6.04 to 24.22. The length of all specimens was 1000 mm. The distance between the two supports (L) was 900 mm. A labelling system was considered for all specimens based on the key features of outer and inner cross-sections. For example, the label 'S76.2 × 6.4-C38.2 × 1.6′ denotes a CFDSAT specimen with an outer tube of 'S76.2 × 6.4′ and an inner tube of 'C38.2 × 1.6′. The notation 'S76.2 × 6.4′ shows that the section is square ('S') with nominal depth and width of 76.2 mm and thickness of 6.4 mm. 'C38.2 × 1.6′ stands for a circular section ('C') with nominal diameter of 38.2 mm and thickness of 1.6 mm. The cross-sections selected in this study are available in the UK market for structural applications. The chosen cross-sectional dimensions have allowed to investigate the effect of hollow ratio and thickness of hollow tube on the flexural capacity of CFDSAT members. For example, specimens C88.6 × 1.6-C19.2 × 3.2 and C88.6 × 1.6-C25.4 × 3.2 were selected to investigate the influence of higher hollow ratio by increasing the diameter of inner tube from 19.2 mm to 25.4 mm and specimens S76.2 × 4.8-S25.4 × 3.2 and S76.2 × 6.4-S25.4 × 3.2 were used to study the effect of larger thickness of outer tube by increasing it from 4.8 mm to 6.4 mm. Finally, the selected cross-sections have provided a sufficient range of experimental data that allows for a subsequent numerical parametric study that generated additional performance data.

During the preparation of CFDSAT specimens, wooden plates were used at the top and bottom ends of the specimens to confirm that the outer and inner tubes were positioned concentrically. The wooden plates were prepared by glueing two parts, i.e., an outer part which had the same dimensions as the outer tube and an inner part which had dimensions similar to the dimension of the gap between the two tubes (Fig. 2(a)). Prior to casting, the top end of inner tubes was covered by strong tape to prevent the concrete to enter inside the inner tube accidentally. The bottom wooden plates were sealed properly to avoid any leakage of concrete. Concrete was filled with layers and the compaction was conducted by a vibrating table. After that, all specimens were enclosed with a plastic cover to avoid any moisture evaporation and cured for 28 days. Fig. 2 presents photographs of the wooden plates and the three different types of cross-sections of test specimens.

2.2. Material testing

2.2.1. Aluminium alloy

Aluminium alloy's material properties were obtained from longitudinal tensile coupon tests. Two coupons were machined longitudinally from each square (flat coupons) and circular (curved coupons) hollow section based on the guidelines set out in BS EN ISO 6892–1 [40]. A 50 kN capacity tensile testing machine was used for the tensile tests (Fig. 3 (a)). The flat coupons were tested using flat grip faces, while for curved coupons, grip faces with a jaw profile were used to ensure a good amount of contact between grip faces and specimens. The tests were conducted using 0.2 mm/min displacement-control load. An extensometer was used to record the longitudinal strains of the coupons. The stress–strain curves obtained during the tests were reproduced using Eqs. (1) and (2) suggested by Ramberg and Osgood [41] and modified by Hill [42].

$$\varepsilon = \frac{f}{\mathrm{E}} + 0.002\left(\frac{f}{f_{0.2}}\right)^{n} \tag{1}$$

$$n = \frac{\ln 2}{\ln\left(\frac{f_{0.2}}{f_{0.1}}\right)} \tag{2}$$

In the above equations, f represents the tensile stress, ε is the tensile strain, $f_{0.1}$ denotes the 0.1 % proof stress, $f_{0.2}$ stands for the 0.2 % proof stress, E is the modulus of Elasticity and n is the exponent of strain hardening. Table 2 summarises the coupon test results, where f_u is the maximum stress at tension, ε_u is the strain at maximum stress and ε_f is the strain at fracture along with the characteristic values of 0.2 % proof stress ($f_{0.2,\mathrm{EC9}}$), the ultimate tensile strength ($f_{u,\mathrm{EC9}}$) and strain hardening exponent (n_{EC9}) recommended by Eurocode 9 (EC9) [43]. It can be observed that the characteristic values of $f_{0.2,\mathrm{EC9}}$ and $f_{u,\mathrm{EC9}}$ are generally a bit higher compared to the values recommended by Eurocode for 6082-T6 alloy. Typical stress–strain curves along with the corresponding Ramberg-Osgood curves of the S25.4 × 3.2 and C19.2 × 3.2 material coupons are presented in Fig. 3(b).

2.2.2. Concrete

The concrete was prepared using cement, fine aggregates, coarse aggregates (less than 10 mm) and normal water. The ratio of 1:1.45:2.49:0.52 by weight was considered for the concrete mixture. The density of concrete was 2380 kg/m^3. The material properties of concrete were obtained from the compressive tests of concrete cubes. Four 100 mm concrete cubes were produced from the same concrete mixture that

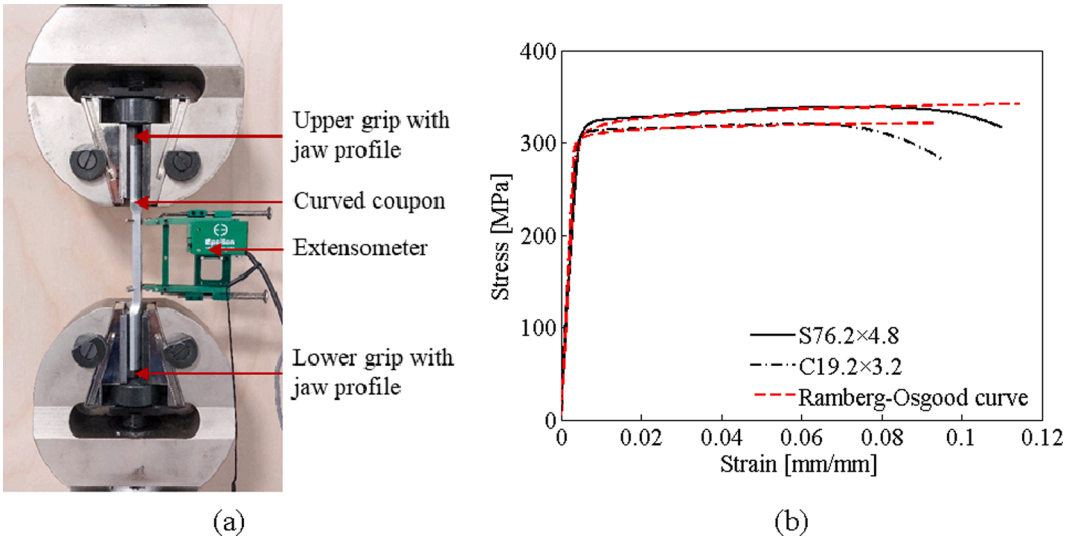

Fig. 3. (a) Photograph of coupon test, (b) Typical test and corresponding Ramberg-Osgood stress–strain curves.

Table 2
Tensile coupon test results.

Specimen	E (MPa)	$f_{0.1}$ (MPa)	$f_{0.2}$ (MPa)	$f_{0.2,EC9}$ (MPa)	f_u (MPa)	$f_{u,EC9}$ (MPa)	ε_u (%) (mm/mm)	ε_f (%) (mm/mm)	n	n_{EC9}
S19.2 × 1.6	72,500	185	189	160	215	195	4.57	5.45	28.83	24
S25.4 × 3.2	70,000	276	283	250	328	290	7.66	16.00	28.06	32
S76.2 × 4.8	70,700	305	311	250	338	290	5.97	11.70	33.91	32
S76.2 × 6.4	68,400	293	298	260	329	310	7.62	18.00	34.80	25
C25.4 × 3.2	71,900	283	289	250	327	290	8.50	13.00	29.58	32
C19.2 × 3.2	72,800	303	306	250	320	290	5.18	8.94	36.53	32
C38.2 × 1.6	72,700	289	295	250	311	290	4.40	7.22	35.48	32
C76.2 × 3.2	69,500	264	270	250	313	290	7.87	13.30	28.92	32
C88.6 × 1.6	68,300	199	203	160	233	195	6.98	12.40	29.02	24

Table 3
Measured concrete cube compressive strengths.

Compressive strength of cubes (MPa)	Mean (MPa)
37.2	36.5
35.7	
36.8	
36.5	

was used for the casting of CFDSAT specimens. The cubes were cured for 28 days and tested according to the guidance of BS EN 12390–3 [44] on the same day of the bending tests. The compressive strengths of concrete cubes are reported in Table 3.

2.3. Four-point bending tests

The CFDSAT specimens were tested in four-point bending arrangement. The specimens were supported by two pinned supports to allow rotation around the bending axis and movement along the longitudinal direction of the specimens. The pinned supports were located 900 mm away from each other. The distance between the support and loading point (shear span) was 300 mm. The gap between the two loading points (moment span) was also 300 mm. The shear span over depth ratio of all specimens was greater than 0.5 to avoid shear failure of the specimens [45]. The bending test was conducted using a 600 kN capacity servo-hydraulic machine. The load was applied using two rollers with a displacement-controlled rate of 1.5 mm/min. At the loading points, steel plates were employed for the square specimens [9] and half-circle steel blocks were used for the circular specimens to avoid any localised failure due to load concentration [1]. During the tests, three 50 mm-stroke linear variable displacement transducers (LVDTs) were applied to record the vertical movement of the specimens, among them one was placed at mid-length and two were positioned under the loading points. At the mid-length of the top and bottom flanges, two strain gauges were used to measure the compressive and tensile strains of the specimens. A data logger was employed to record all data during the tests. Fig. 4 presents photographs and a schematic drawing of the experimental set-up.

3. Four-point bending test results

Typical failure modes of CFDSAT specimens observed from the bending tests are presented in Figs. 5 and 6 and reported in Table 4. The predominant observed failure mode was yielding (Fig. 5(a)). Besides yielding, some circular specimens (i.e., C88.6 × 1.6-C19.2 × 3.2, C88.6 × 1.6-C25.4 × 3.2 and C88.6 × 1.6-C38.2 × 1.6) experienced small outward local buckling at the top face of outer tube within the two loading points (Fig. 5(b)). However, no inward bulging was observed at the outer tube of any specimen which is attributed to the infilled concrete that efficiently delayed the occurrence of outward buckling and prevented the formation of inward buckling. Moreover, in some circular specimens (i.e., C88.6 × 1.6-C19.2 × 3.2, C88.6 × 1.6-C25.4 × 3.2 and C88.6 × 1.6-C38.2 × 1.6) fracture of the outer tube was noticed at the tension side after they reached their flexural capacity (Fig. 6(a)).

To investigate the failure pattern of the concrete infill and the inner profile, the outer profile and concrete infill were partly removed after the bending test. Fig. 5(c) and Fig. 6(b) illustrate the failure pattern of the inner tube and concrete infill of a typical specimen, respectively. It can be found from Fig. 5(c) that, similarly to the outer tube the inner tube exhibited obvious bending deformation. However, no tensile fracture or local buckling was noticed in the inner tube of the examined specimens. Fig. 6(b) shows that a number of flexural cracks occurred parallelly in the tension region of concrete along the moment span. The cracks developed uniformly and propagated from tension to the compression region. In the moment span, no diagonal crack of concrete is noticed, which indicates that shear force was not developed during the tests.

A typical bending moment versus mid-span deflection/longitudinal strain curve of the specimens is shown in Fig. 7 indicating different stages appeared during the test. The deflection and longitudinal strain data recorded from the LVDT and strain gauge positioned at the mid-span of the bottom flange were used for the curve. Note that the locations of initiation of the tensile cracks in concrete infill and outward local buckling of outer tube in the curve were identified using FE analysis (Fig. 7(b) and (c)). The yielding point of the aluminium alloy is indicated by the yield strain measured during the tensile test of the respective coupons. The bending moment (M) and curvature (κ) of all the specimens were determined using Eqs. (3) and (4), respectively.

$$M = \frac{PL}{6} \tag{3}$$

$$\kappa = \frac{8(\delta - \delta_{av})}{4(\delta - \delta_{av})^2 + L_l^2} \tag{4}$$

where P is the applied load during the tests, δ and δ_{av} are the mid-span displacement and average vertical displacement of two loading points at the ultimate moment, respectively. L and L_l are the distance between the supports and the loading points, respectively.

Fig. 8 presents the bending moment versus mid-span deflection/bottom longitudinal strain curves of all specimens. The figure illustrates that initially, all curves exhibit a linear relationship between mid-span deflection/longitudinal strain and bending moment, indicating that the material of CFDSAT sections was in the elastic stage. At this stage, the cracks of concrete infill appear at the tensile region and the aluminium alloy starts to yield when the moment reaches points A and B, respectively. After this stage, the curves deviate from the initial linearity and start to exhibit nonlinear behaviour as they enter the elastic–plastic stage. At the plastic stage, the curves of all specimens show an almost flat yield plateau with increasing displacement. In this region, specimens C88.6 × 1.6-C19.2 × 3.2, C88.6 × 1.6-C25.4 × 3.2 and C88.6 × 1.6-C38.2 × 1.6 experienced outward local buckling at the outer tubes as they fall in Class 4 category according to EC9 [43]. Point C shows the location in the curve where the local buckling starts to appear. It can be observed that the small outward local buckling appeared at the plastic stage before the bending moment reached the flexural strength of

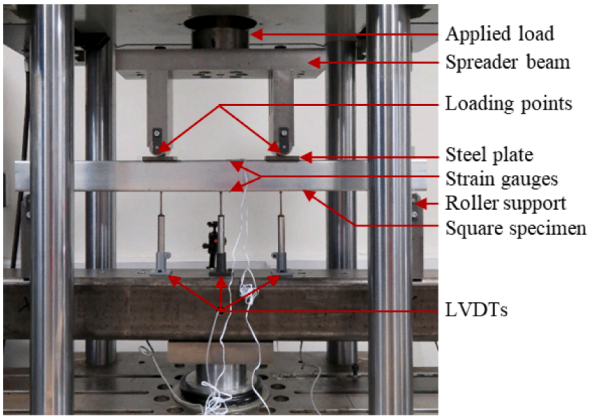

(a) Square CFDSAT specimen test set-up

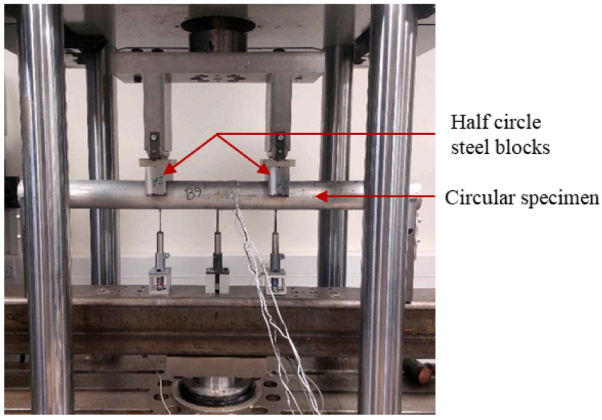

(b) Circular CFDSAT specimen test set-up

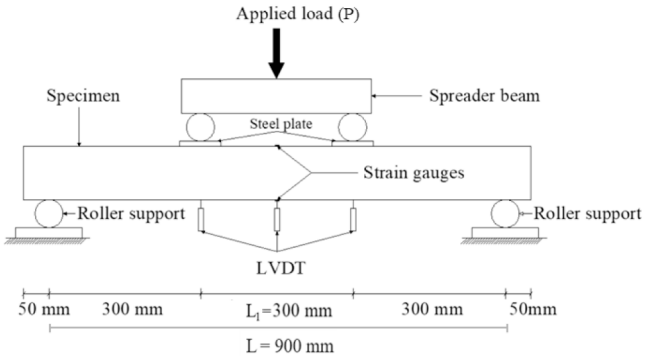

(c) Schematic drawing of square CFDSAT specimen test set-up

Fig. 4. Photographs and a schematic drawing of the experimental set-up.

these specimens. However, the effect of local buckling was minimised as the concrete infill restrained the formation of inward buckling and delayed the development of outward buckling. Moreover, at this stage, these specimens failed due to tensile fracture of the outer tube which is indicated by point D. No descending branch or sudden drop appears in the curve of other specimens in the plastic region. In these cases, the tests were terminated at a large vertical displacement of 60 mm (i.e., $L/15$) and the recorded bending moment at that displacement was taken as the flexural strength of the corresponding specimens. The same approach was adopted in previous research [9]. It can be observed from Fig. 8 that all CFDSAT specimens demonstrated good ductile response which is attributed to the beneficial composite behaviour of the three

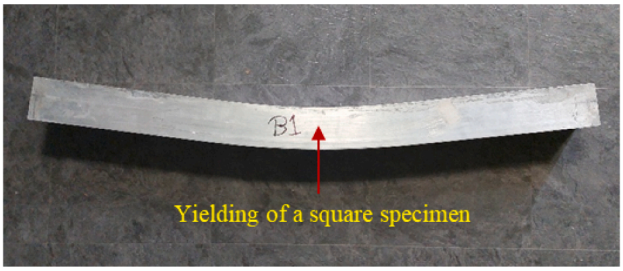

(a) S76.2×6.4-S25.4×3.2

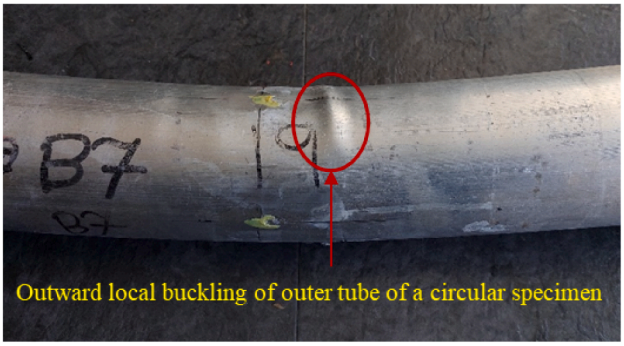

(b) C88.6×1.6-C25.4×3.2

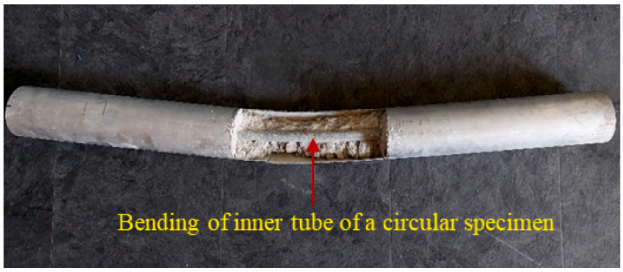

(c) C88.6×1.6-C19.2×3.2

Fig. 5. Typical failure modes. (a) Yielding of a square specimen, (b) Local outward buckling of the outer tube of a circular specimen, (c) Bending of the inner tube of a circular specimen.

components of the CFDSAT sections. The flexural strength ($M_{u,Test}$) and curvature (κ) of all test specimens are reported in Table 4. It can be observed from this table that the flexural strength of CFDSAT specimens increased significantly with the increase of thickness of the outer tube when the inner tube dimensions remain the same. For example, the flexural strength of specimen S76.2 × 6.4-S25.4 × 3.2 enhanced by 23.3 % compared to specimen S76.2 × 4.8-S25.4 × 3.2 as the thickness of the outer tube of the former one increased from 4.8 mm to 6.4 mm. Moreover, it is also noticed that the flexural strength of CFDSAT specimens improved due to increase the dimensions of the inner tube when the outer tube dimensions are constant, however, the enhancement is not prominent. For example, when the outer diameter of inner tube increased from 19.2 mm to 25.4 mm, the flexural strength of specimen C88.6 × 1.6-C19.2 × 3.2 improved moderately, i.e., around 5 % compared to the strength of specimen C88.6 × 1.6-C25.4 × 3.2. The effect of cross-sectional dimensions of the outer and inner tubes on the flexural capacity of CFDSAT specimens is further investigated by FE analyses and discussed in Section 4.3.

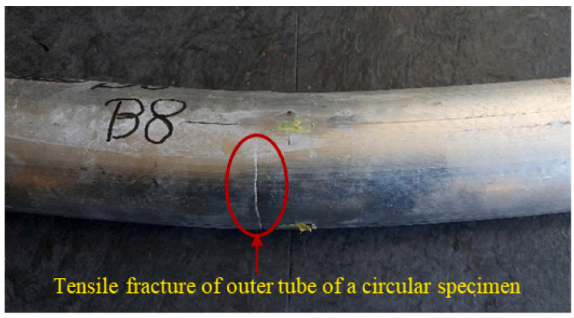

(a) C88.6×1.6-C38.2×1.6

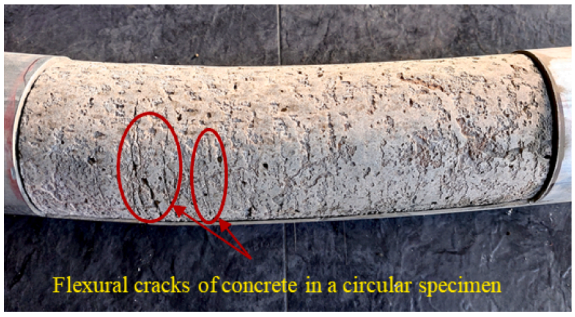

(b) C88.6×1.6-C19.2×3.2

Fig. 6. (a) Tensile fracture of the outer tube of a circular specimen, (b) Flexural cracks of concrete in a circular specimen.

Table 4
Failure modes and flexural strength of CFDSAT specimens.

Specimen	Failure mode	$M_{u,Test}$ (kNm)	κ (mm^{-1})
S76.2 × 6.4-S19.2 × 1.6	Y	17.37	0.0014
S76.2 × 6.4-S25.4 × 3.2	Y	18.35	0.0012
S76.2 × 4.8-S25.4 × 3.2	Y	14.88	0.0011
S76.2 × 6.4-C25.4 × 3.2	Y	18.18	0.0012
S76.2 × 6.4-C38.2 × 1.6	Y	18.25	0.0011
C88.6 × 1.6-C19.2 × 3.2	Y + LB + TF	4.74	0.0008
C88.6 × 1.6-C25.4 × 3.2	Y + LB + TF	5.02	0.0010
C88.6 × 1.6-C38.2 × 1.6	Y + LB + TF	4.84	0.0009
C76.2 × 3.2-C25.4 × 3.2	Y	7.62	0.0009
C76.2 × 3.2-C38.2 × 1.6	Y	7.71	0.0009

Note. Y = Yielding, LB = Local buckling of outer tube, TF = Tensile fracture

4. Numerical investigation

A numerical study of the flexural response of CFDSAT specimens was conducted using the ABAQUS software [46]. Finite element (FE) models were developed by taking into account the geometric and material nonlinearities. The model was validated based on the experimental results and used to conduct a parametric study.

4.1. FE modelling

FE models were developed utilizing the measured geometric dimensions and material properties listed in Tables 1, 2 and 3. The outer and inner tubes were modelled using four-node shell elements (S4R) [47–49] and the concrete infill was simulated considering eight-node solid elements (C3D8R) [9,50,51]. To select the optimum size of S4R and C3D8R elements, a mesh sensitivity study was performed. It was noticed that an average mesh size of 5 mm (L/180) is appropriate in terms of accuracy of results and analysis time. Therefore, the structure was discretized using 5 mm element size and using the structured meshing method.

The elastic–plastic material relationship was applied to model the mechanical behaviour of aluminium sections. The elastic behaviour of aluminium was simulated by inputting the modulus of Elasticity reported in Table 2 and the Poisson's ratio of 0.33. The plastic behaviour was considered by applying the von Mises plasticity criterion with isotropic hardening. The engineering stress-plastic strain values found from the tensile coupon tests were transformed to true stress-logarithmic plastic strain values and entered in ABAQUS. The mechanical response of concrete was considered by utilizing the concrete damage plasticity (CDP) model. The concrete's modulus of Elasticity was determined using the formula given in EC4 [39] and the Poisson's ratio value was considered equal to 0.2. In the CDP model, the values of 40°, 0 and 0.1 were used for the dilation angle, the viscosity parameter and the flow potential eccentricity, respectively [52]. The compressive meridian was calculated by the formula recommended by Yu et al. [53] and the ratio of the compressive strength because of biaxial loading over uniaxial compressive strength was calculated by the equation suggested by Papanikolaou and Kappos [54]. In the FE analyses, the confined concrete model suggested by Tao et al. [52] (Fig. 9) was employed to consider the confinement effect offered by the outer and inner profiles on the compressive response of the concrete infill. Tao et al. [52] originally suggested and calibrated the model for fully concrete-filled steel tubular stub columns. In concrete-filled double skin metal tubular sections, the inward deformation of concrete is restricted by the inner tube, thus it is assumed that the compressive response of concrete infill of these sections is similar to the concrete confined by only the outer tube [55]. Therefore, the uniaxial compressive stress–strain response for concrete infill of CFST section [52] is used in this study with the modified confinement factor suggested by the authors [20,21,56] for concrete-filled double skin metal sections. The tensile response of concrete infill was considered by a linear tensile stress–strain relationship up to 10 % of the compressive strength of concrete [52] and a post-peak curve based on fracture energy [57–59].

The interaction between the aluminium hollow sections and concrete infill was considered using surface-to-surface contact in ABAQUS. The inner surfaces of outer tubes and outer surfaces of inner tubes were set as slave surfaces, whereas the outer and inner surfaces of concrete were assigned as master surfaces. In the normal direction, hard contact was used to allow separation during tensile force and prevent penetration under compressive force. Coulomb friction behaviour was adopted in the horizontal direction, with a value of friction coefficient of 0.3 for permitting slippage between the surfaces [9]. Due to the heat-treatment process, the generation of residual stresses of aluminium alloy is very low [7]. The initial local geometric imperfection has no considerable influence on the flexural behaviour of concrete-filled double skin metal sections because of the existence of concrete infill [1]. Therefore, the influence of residual stresses and initial local geometric imperfections were not taken into account in the FE analyses. The pinned support conditions were modelled by considering rotation around the bending axis (X direction) and translation in the longitudinal direction of the beam (Z direction). The load was applied along the vertical direction (Y direction) at the loading points using the displacement control technique. Fig. 10 presents the geometry, boundary and loading conditions of a typical FE model.

4.2. Model validation

FE model was validated by comparing the FE flexural strength, bending versus moment-mid-span deflection relationship and failure modes with the corresponding results obtained from the experiments. Table 5 presents the ratios of the flexural strength of all specimens obtained from the FE analyses over the corresponding ones from the bending tests ($M_{u,FE}/M_{u,Test}$). It is found that the developed FE model correctly determines the flexural capacity of the CFDSAT specimens

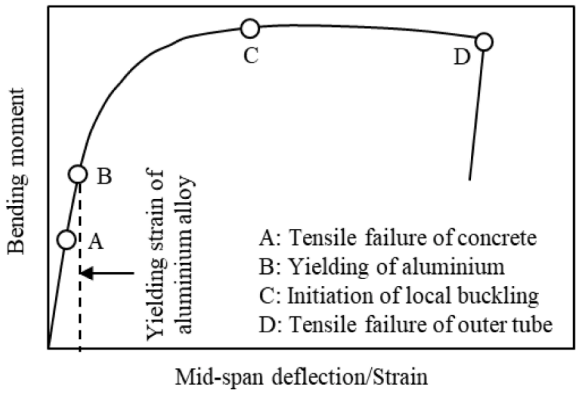

(a) Typical bending moment versus mid-span deflection/longitudinal strain curve

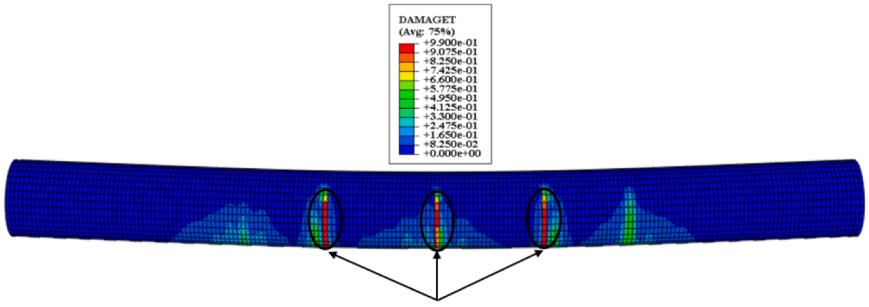

(b) Point A: Tensile failure of concrete

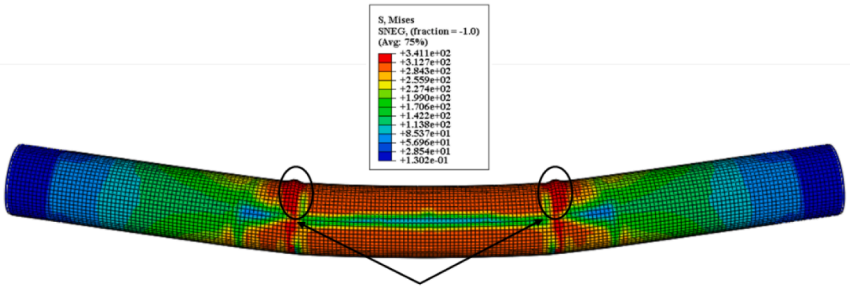

(c) Point C: Initiation of local buckling of outer tube

Fig. 7. Typical bending moment versus mid-span deflection/longitudinal strain curve indicating different stages appeared during the test.

with mean and coefficient of variation (COV) of $M_{u,FE}/M_{u,Test}$ equal to 1.01 and 0.05, respectively. However, for some specimens with circular outer sections, the FE flexural strength is slightly higher compared to the test results. This may happen if the material properties obtained from the coupon tests are higher than the actual ones of respective specimens. During measuring the geometry of the curved coupons, general purpose measuring tools, i.e., tape and slide calliper, were used which may have led to smaller values than the proper ones. Hence, the estimated cross-section area of the curved gauge section may have been less than the actual area, resulting in higher tensile stress values compared to the real values. In Fig. 11, FE and experimental bending moment versus mid-span deflection curves are compared for two typical specimens, where good agreement is observed between the curves. Fig. 12 illustrates the comparison of failure modes of some specimens observed from the bending tests and FE analyses, again showing accurate replication of the deformation profile and failure modes of CFDSAT specimens. On the basis of the above observations, it can be concluded that the developed FE models can accurately capture the structural response of CFDSAT beams.

4.3. Parametric study

The validated FE model was adopted to conduct a parametric study for examining the influence of hollow ratio, cross-section slenderness of the outer and inner sections, concrete strength, cross-section shape and composite action on the flexural behaviour of CFDSAT specimens. The average material properties found from flat and curved coupons were used for square and circular aluminium tubes, respectively. In total 94

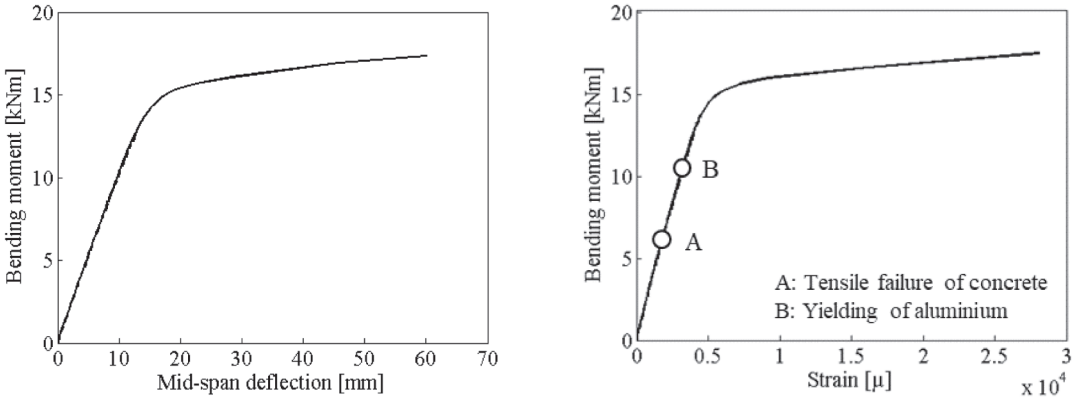

(a) S76.2×6.4-S19.2×1.6

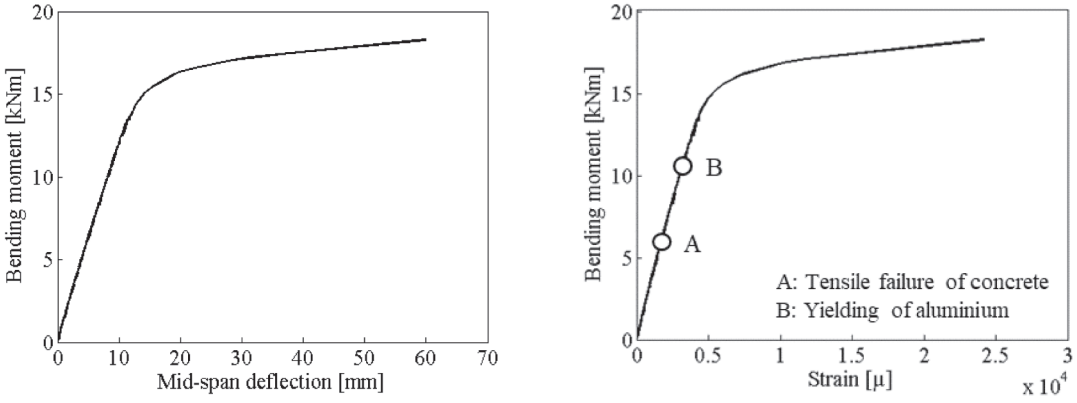

(b) S76.2×6.4-S25.4×3.2

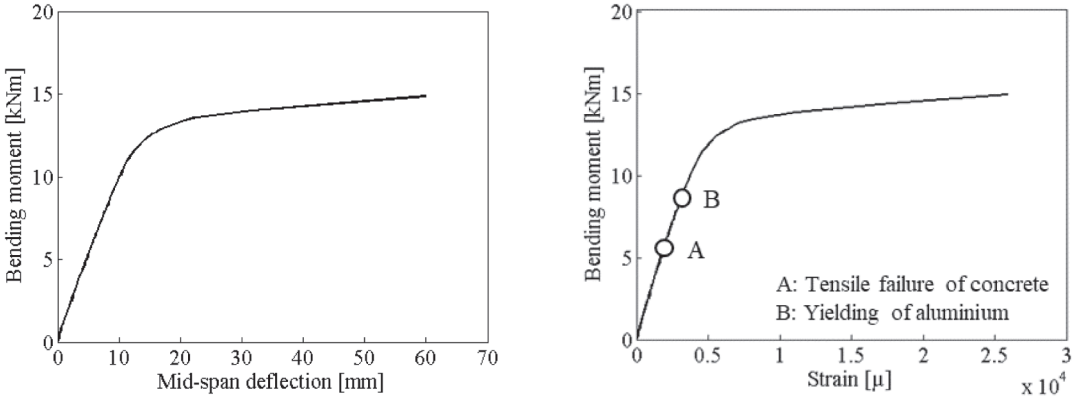

(c) S76.2×4.8-S25.4×3.2

Fig. 8. Bending moment versus mid-span deflection/longitudinal strain curves of CFDSAT specimens.

CFDSAT specimens were modelled, considering different combinations of outer and inner cross-section shapes, i.e., square-square, square-circular, circular-circular and circular-square. Outer tubes with cross-sectional dimensions of 60 × 60, 75 × 75, 100 × 100 and 120 × 120 mm^2 for square sections and diameters of 60, 75, 100 and 120 mm for circular sections were considered with wall thickness varied from 1 to 8 mm. Inner tubes with cross-sectional dimensions of 20 × 20, 25 × 25, 30 × 30 and 35 × 35 mm^2 for square sections and diameter of 20, 25, 30 and 35 mm for circular sections were considered with wall thickness ranging from 1 to 5 mm. Three different concrete cube compressive strengths of 30, 40 and 50 MPa were considered in this study.

4.3.1. Effect of hollow ratio

The influence of hollow ratio on the flexural behaviour CFDSAT

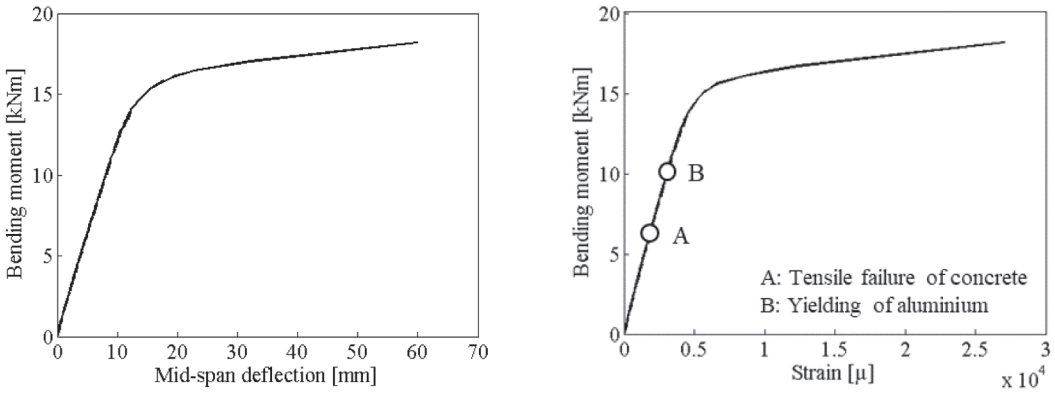

(d) S76.2×6.4-C25.4×3.2

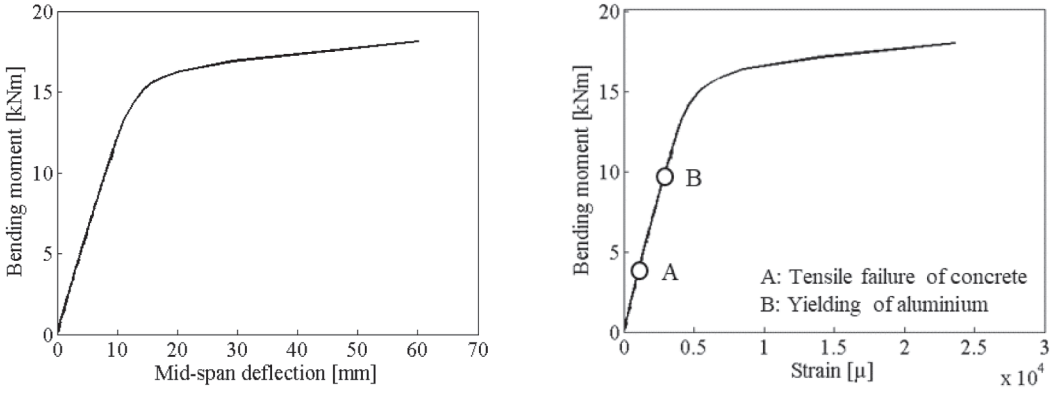

(e) S76.2×6.4-C38.2×1.6

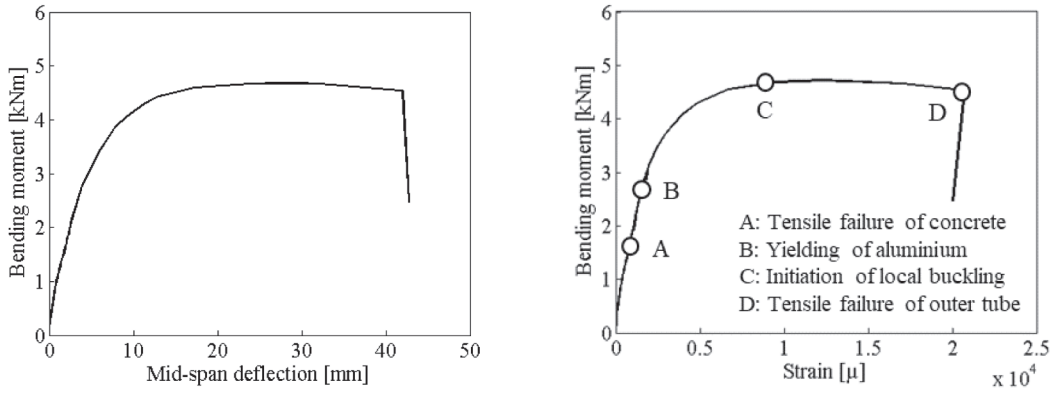

(f) C88.6×1.6-C19.2×3.2

Fig. 8. (*continued*).

specimen was investigated by changing the depth/diameter of inner and outer tube. The hollow ratio is determined by Eq. (5).

$$\alpha = \frac{D_i}{D_o - 2t_o} \tag{5}$$

Hollow ratios (α) varying from 0.17 to 0.80 were considered for both square and circular CFDSAT specimens. Fig. 13 presents the effect of α on the bending moment versus midspan deflection curves of typical CFDSAT specimens. Similar to the experimental observations it can be found from Fig. 13(a) that when the dimensions of the inner tube are constant, the flexural strength of CFDSAT specimens remarkably increased with the decrease of α (i.e., increase of depth/diameter of outer tube). This can be attributed to the fact the larger depth/diameter of outer tube offers higher moment of inertia of the outer tube as well as larger concrete area, which lead to the enhancement of the bending capacity. The flexural strength of CFDSAT specimens also improved with the increase of inner tube depth/diameter by maintaining same outer tube (i.e., increase of α), however, the improvement is not prominent (Fig. 13(b)). This finding also matched with the experimental observation. This is because the influence of inner tube is less on the overall

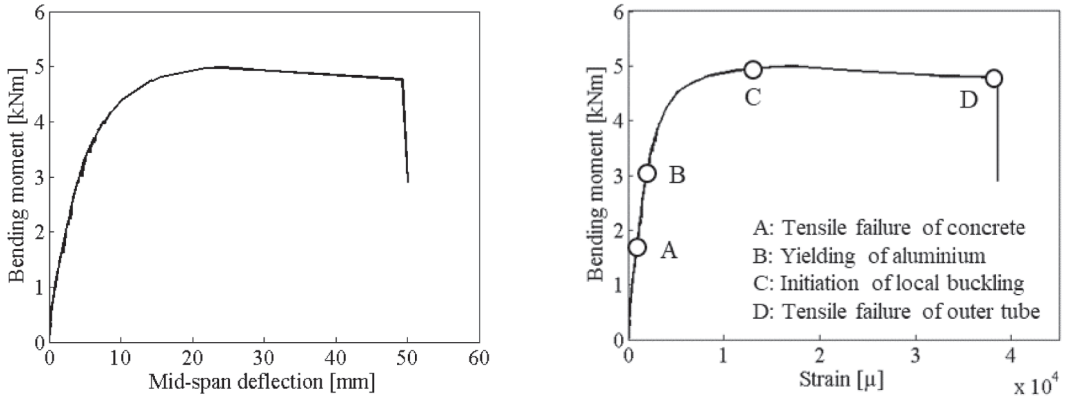

(g) C88.6×1.6-C25.4×3.2

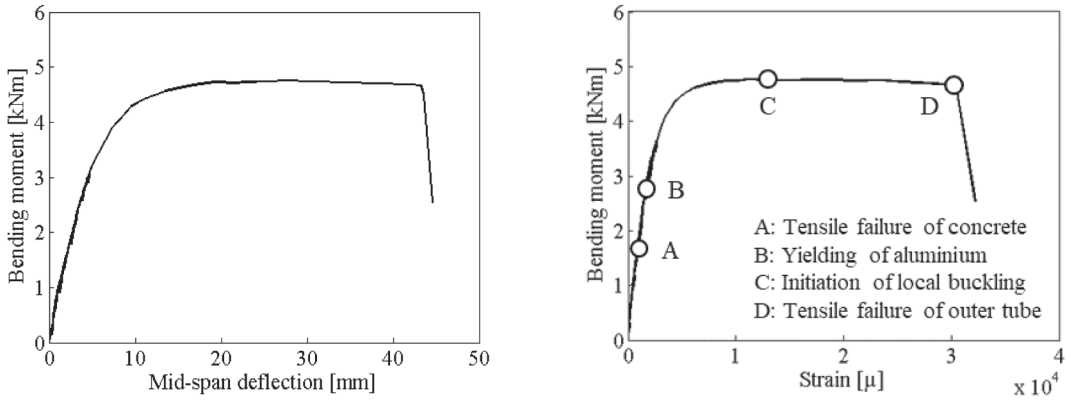

(h) C88.6×1.6-C38.2×1.6

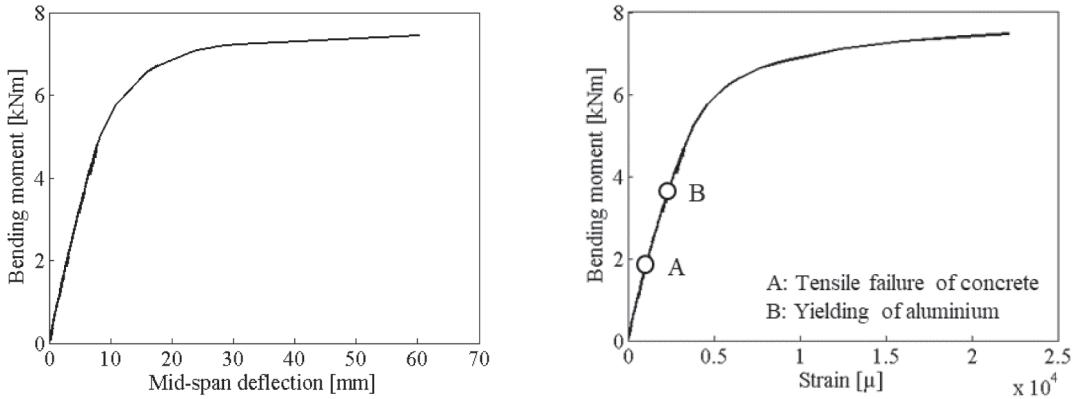

(i) C76.2×3.2-C25.4×3.2

Fig. 8. (*continued*).

flexural strength of CFDSAT specimens. This is demonstrated for typical specimens in Fig. 14(a) and (b), where the moment contribution of each of the three sections (outer and inner aluminium tubes and concrete infill) is presented, showing a smaller contribution of the inner tube compared to the outer one and concrete infill. A similar observation is presented in a previous study on the structural response of CFDSST beams [1].

4.3.2. Effect of depth/diameter to thickness ratio of the outer tube

Fig. 15 presents the effect of depth/diameter to thickness ratio of the outer tube (D_o/t_o) on the bending moment versus midspan deflection curves of typical CFDSAT beams. D_o/t_o values ranging from 7.5 to 120 for both square and circular sections were considered by altering the thickness of the outer tube. It can be observed from the figure that the D_o/t_o ratio has a considerable influence on the flexural strength of CFDSAT specimens as decreasing D_o/t_o ratio noticeably increased the flexural strength of the specimens. This can be attributed to the fact that,

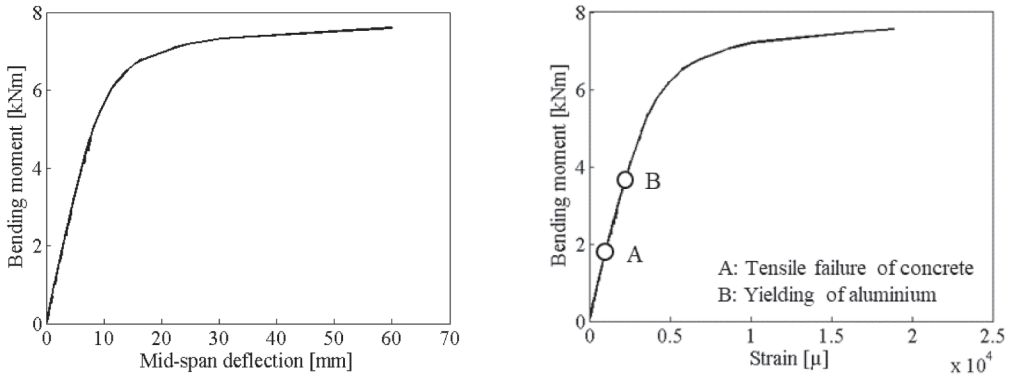

(j) C76.2×3.2-C38.2×1.6

Fig. 8. (*continued*).

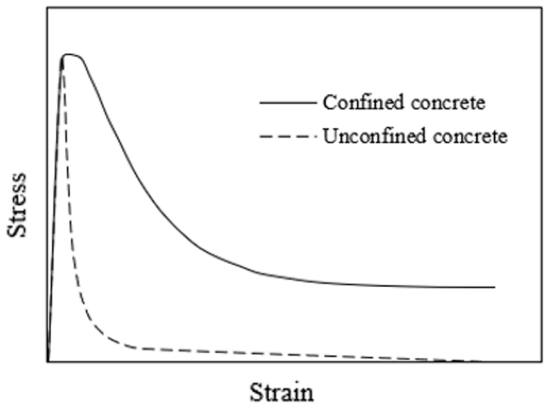

Fig. 9. Compressive response of confined concrete [52].

by decreasing D_o/t_o ratio (i.e., larger thickness) the moment of inertia of the outer section increases, enhancing the overall flexural resistance of the specimens.

4.3.3. *Effect of depth/diameter to thickness ratio of the inner tube*

The effect of depth/diameter to thickness ratio of the inner tube (D_i/t_i) on the flexural behaviour of CFDSAT specimens is presented in Fig. 16. The D_i/t_i ratio varied from 4 to 35 and this was achieved by changing the thickness of the inner section of square and circular specimens. Fig. 16 illustrates that by decreasing the D_i/t_i ratio the flexural strength of the CFDSAT specimens enhanced slightly, as the larger thickness of the inner section offers higher moment of inertia to the inner tube. However, the effect of D_i/t_i is less significant, as the inner tube provides the least bending resistance among the three components of CFDSAT specimens (Fig. 14(a) and (b)).

4.3.4. *Effect of concrete compressive strength*

To investigate the effect of the concrete grade on the flexural strength of CFDSAT specimens, three different concrete cube compressive strengths (f_{cu}), i.e., 30, 40 and 50 MPa were considered in the parametric study. Fig. 17 shows the effect of the concrete grade on the bending moment versus midspan deflection curves of typical CFDSAT specimens. It is found from the figure that by increasing the concrete strength, the flexural strength of the specimens increased very moderately. This is related to the fact that under in-plane bending, the concrete beneath the neutral axis, is in tension and the higher concrete grade offers a minor contribution to the enhancement of the tensile strength of concrete. Therefore, increasing concrete strength has less influence on the improvement of flexural strength of the CFDSAT specimens.

4.3.5. *Effect of cross-section shape and composite action*

The effect of cross-section shape on bending moment versus midspan deflection curve is presented in Fig. 18. A square and a circular CFDAT specimen with the same cross-section area were considered to study the cross-section shape effect on the flexural strength of the composite beams. It can be noticed from Fig. 18 that the initial stiffness is not influenced by changing the cross-section shape of the specimens. However, the flexural strength of the circular specimen improved slightly than the square one, thus indicating that the circular cross-section offers relatively stronger confinement compared to the square cross-section.

In order to study the composite action between aluminium and concrete, Fig. 19 presents the contact stresses generated at different locations of the mid-span cross-section of typical specimens. It can be observed that initially, the contact stress is small due to the difference in Poisson's ratio between the hollow tubes and the concrete infill. With the increase of the bending moment and the corresponding increase of the specimen's deflection, the contact stresses between the concrete infill and hollow tubes increase as well and the concrete interacts with the hollow tubes. It is clear from the figure that the confining pressure provided by the outer section (points 1 and 4) is higher than the inner section (points 2 and 3), as the outer tube exerts more resistance to the lateral strain of concrete compared to the inner one. Moreover, it is also noticed from the figure that point 4 experiences maximum contact stress, as the large deformation occurring in the concrete's tension zone results in additional pressure between the two materials.

5. Design recommendations

The existing European standards for composite structures, i.e., EC4 [39] strictly provide design guidelines for fully filled carbon steel composite flexural members. However, no design rules are available for the design of CFDSAT flexural members. Therefore, in this section, modifications of EC4 are proposed for the design of CFDSAT flexural members. In sub-section 5.1, a design methodology for determining the flexural strength of square and circular CFDSAT beams is proposed. In sub-section 5.2, the applicability of the proposed design methodology is assessed. Finally, in sub-section 5.3, slenderness limits for square and circular CFDSAT cross-sections are proposed by analysing the test and FE data.

5.1. *Design methodology for CFDSAT beams based on EC4 [39]*

In EC4 [39], the design equation for determining the plastic moment resistance of CFST members is provided based on the plastic stress distribution method (PSDM). In this study, the PSDM was adopted to calculate the plastic moment resistance (M_{pl}) which is considered the theoretical flexural strength ($M_{u,prop}$) of square and circular CFDSAT

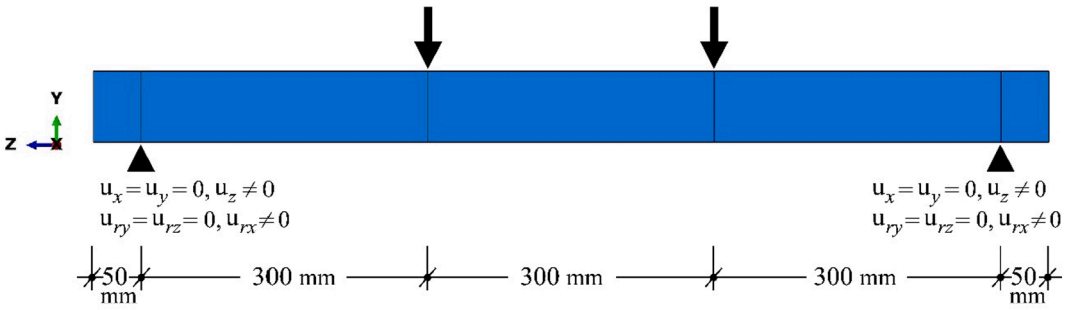

(a)

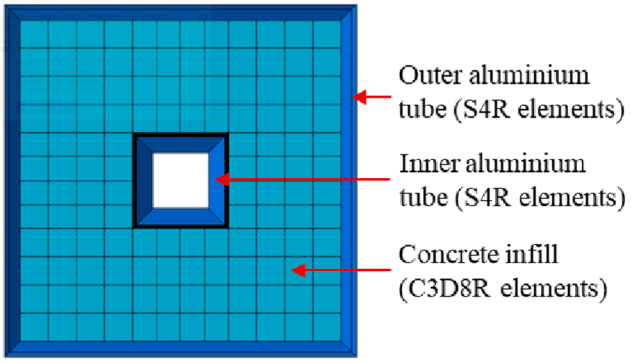

(b)

Fig. 10. FE model. (a) boundary conditions at supports and loading direction, (b) cross-section.

Table 5
Comparison of the FE flexural strength with the corresponding test flexural strength.

Specimen	$M_{u,FE}/M_{u,Test}$
S76.2 × 6.4-S19.2 × 1.6	0.98
S76.2 × 6.4-S25.4 × 3.2	0.95
S76.2 × 4.8-S25.4 × 3.2	0.96
S76.2 × 6.4-C25.4 × 3.2	0.94
S76.2 × 6.4-C38.2 × 1.6	0.99
C88.6 × 1.6-C19.2 × 3.2	1.04
C88.6 × 1.6-C25.4 × 3.2	1.06
C88.6 × 1.6-C38.2 × 1.6	1.09
C76.2 × 3.2-C25.4 × 3.2	1.01
C76.2 × 3.2-C38.2 × 1.6	1.05
Mean	1.01
COV	0.05

specimens. Fig. 20 illustrates the plastic stress distribution of outer and inner aluminium sections and the concrete infill of a CFDSAT section. It is assumed that under compression and tension both outer and inner aluminium sections are able to achieve their yield stress, which are denoted as $f_{0.2,o}$ and $f_{0.2,i}$, respectively. In the compression zone, it is assumed that concrete can reach its full compressive cylinder strength because of the confinement provided by the hollow tubes. However, in the tension zone, the contribution of concrete infill is ignored.

Using PSDM, the following equation was derived to determine the flexural strength of square and circular CFDSAT sections.

$$M_{u,prop} = M_{pl} = \left(W_{pla_o} - W_{pla_o,n}\right)f_{0.2,o} + \left(W_{pla_i} - W_{pla_i,n}\right)f_{0.2,i} + 0.5\left(W_{plc} - W_{plc,n}\right)f_c \quad (6)$$

where W_{pla_o}, W_{pla_i} and W_{plc} are the plastic moduli of the outer and inner aluminium sections and concrete infill, respectively. $W_{pla_o,n}$, $W_{pla_i,n}$ and $W_{plc,n}$ denote the plastic moduli of the outer and inner aluminium sections and concrete infill at $2h_n$, respectively. The term h_n represents the distance of plastic neutral axis from the centre line of the cross-section. The h_n was calculated by considering the equilibrium condition of axial forces in the CFDSAT section. The cross-section classification proposed by EC9 [43] was adopted for classifying the studied aluminium alloy cross-sections. For square sections, the following Eqs. (7)–(13) were used to determine the values of the terms used in Eq. (6).

$$W_{pla_o} = \frac{B_o D_o^2}{4} - \frac{(B_o - 2t_o)(D_o - 2t_o)^2}{4} \quad (7)$$

$$W_{pla_i} = \frac{B_i D_i^2}{4} - \frac{(B_i - 2t_i)(D_i - 2t_i)^2}{4} \quad (8)$$

$$W_{plc} = \frac{(B_o - 2t_o)(D_o - 2t_o)^2}{4} - \frac{B_i D_i^2}{4} \quad (9)$$

$$W_{pla_o,n} = B_o h_n^2 - (B_o - 2t_o)h_n^2 \quad (10)$$

$$W_{pla_i,n} = B_i h_n^2 - (B_i - 2t_i)h_n^2 \quad (11)$$

$$W_{plc,n} = (B_o - 2t_o - B_i)h_n^2 \quad (12)$$

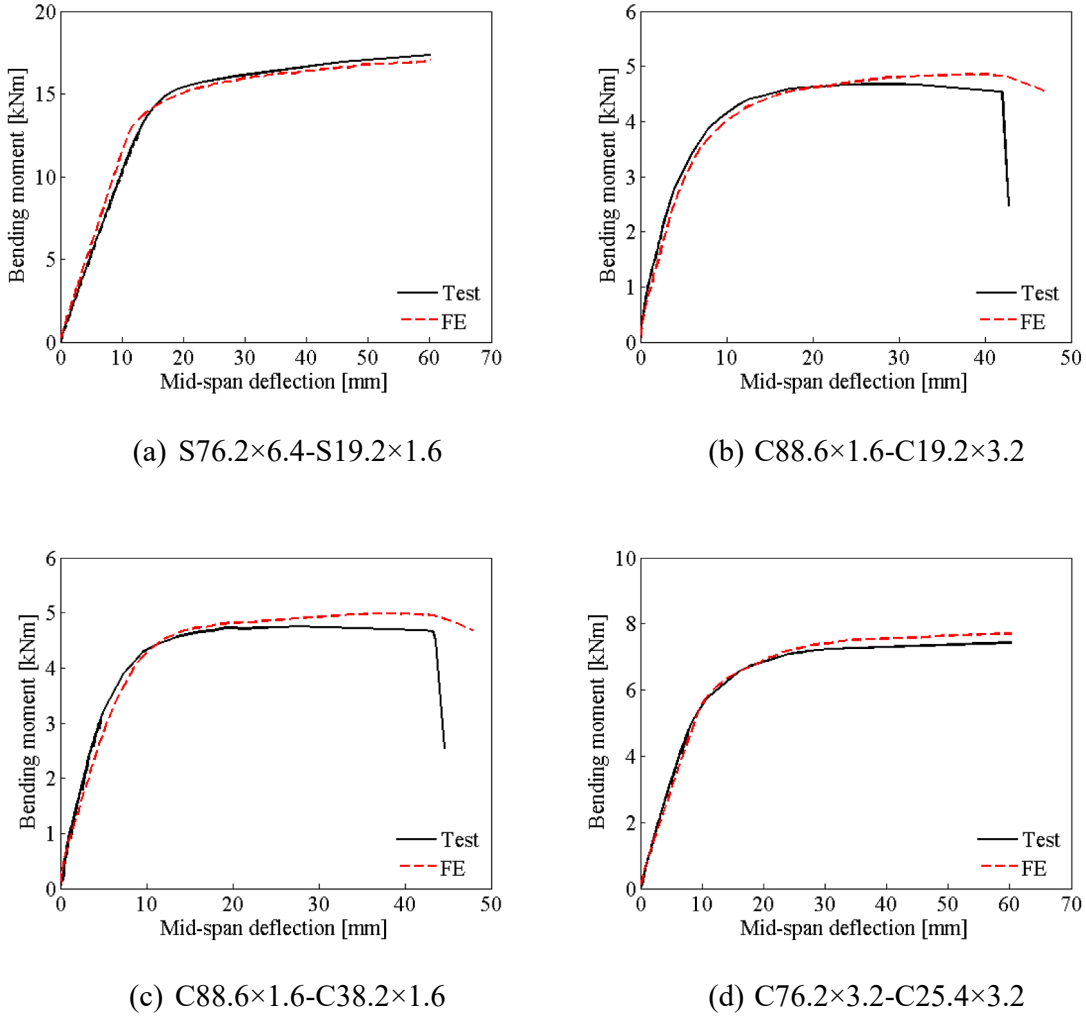

Fig. 11. Comparison of test and FE bending moment-midspan deflection curves.

$$h_n = \frac{A_c f_c}{2(B_o - B_i)f_c + 4t_o\left(2f_{0.2,o} - f_c\right) + 4t_i\left(2f_{0.2,i}\right)} \tag{13}$$

where A_c is area of concrete and f_c is the compressive cylinder strength of concrete, which is considered 80 % of the compressive cube strength of concrete (f_{cu}).

For circular sections, the following Eqs. (14)–(20) were applied to calculate the values of the terms used in Eq. (6).

$$W_{pla_o} = \frac{D_o^3}{6} - \frac{(D_o - 2t_o)^3}{6} \tag{14}$$

$$W_{pla_i} = \frac{D_i^3}{6} - \frac{(D_i - 2t_i)^3}{6} \tag{15}$$

$$W_{plc} = \frac{(D_o - 2t_o)^3}{6} - \frac{D_i^3}{6} \tag{16}$$

$$W_{pla_o,n} = D_o h_n^2 - (D_o - 2t_o)h_n^2 \tag{17}$$

$$W_{pla_i,n} = D_i h_n^2 - (D_i - 2t_i)h_n^2 \tag{18}$$

$$W_{plc,n} = (D_o - 2t_o - D_i)h_n^2 \tag{19}$$

$$h_n = \frac{A_c f_c}{2(D_o - D_i)f_c + 4t_o\left(2f_{0.2,o} - f_c\right) + 4t_i\left(2f_{0.2,i}\right)} \tag{20}$$

5.2. Flexural strength of CFDSAT beams

The applicability of the suggested design rule is evaluated by comparing the predicted design flexural strength ($M_{u,prop}$) with the flexural strength obtained from the test and FE results (M_u). The ratios of the test and FE flexural strength over the predicted flexural strength ($M_u/M_{u,prop}$) along with their mean and COV values are listed in Table 6. The mean and COV values of $M_u/M_{u,prop}$ are equal to 1.05 and 0.08, respectively. This implies that the proposed methodology based on EC4 provides a good and safe prediction of the flexural strength of CFDSAT specimens. In order to evaluate the cross-section effect, the cross-section class of the outer and the inner tubes has been added in Table 6. It is noticed that the proposed methodology based on EC4 [39] works better for the outer cross-sections that fall in Class 4 category proposed by EC9 [43] for aluminium structural members (e.g., for C88.6 × 1.6). This may indicate that the effective thickness method adopted by EC9 [43] for Class 4 cross-sections combined with EC4 provides an accurate prediction of the flexural capacity of CFDSAT beams. Fig. 21 presents the comparisons between the predicted strength and strength obtained from the tests and FE analyses. It is also demonstrated that the proposed methodology is quite accurate as almost all the points are close to the diagonal line (i.e., $M_u/M_{u,prop}$ equal to unity). On the basis of the above comparisons, it can be concluded that the suggested design methodology is appropriate to predict the flexural strength of CFDSAT sections.

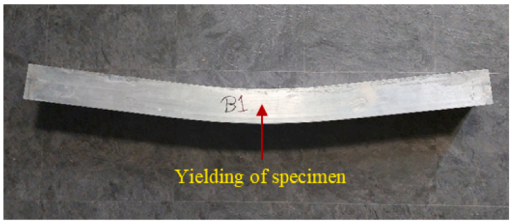

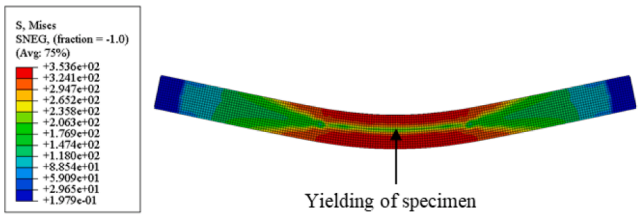

(a) S76.2×6.4-S19.2×1.6

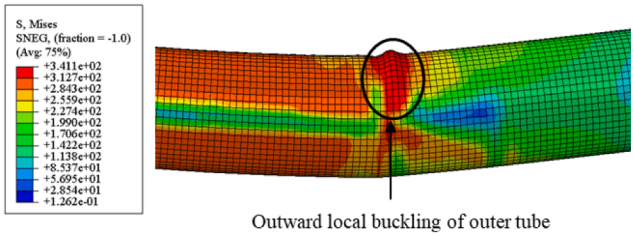

(b) C88.6×1.6-C25.4×3.2

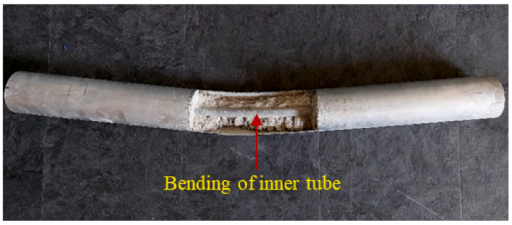

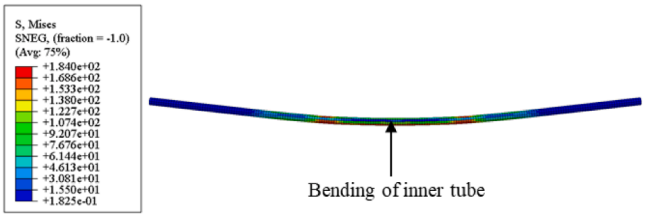

(c) C88.6×1.6-C19.2×3.2

Fig. 12. Comparison of test and FE failure modes.

5.3. Slenderness limits for CFDSAT cross-section

In EC4 [39], slenderness limits are provided for CFST cross-sections and it is suggested that the effect of local buckling needs to be accounted for those sections which exceed these limits. The maximum permitted value of the cross-sectional slenderness is 52 $\sqrt{235/f_{0.2}}$ for square sections and 90 $(235/f_{0.2})$ for circular sections. However, no slenderness limits are available for CFDSAT cross-sections due to lack of data. Hence, in this section, the slenderness limits for square and circular CFDSAT cross-sections are recommended based on the test and FE results. To obtain these limits, the ratio of experimentally/numerically obtained flexural strength (M_u) over the plastic moment capacity (M_{pl}) calculated from Eq. (6), is plotted against the cross-section slenderness parameter β/ε in Fig. 22(a) for square CFDSAT sections and against β/ε^2 in Fig. 22 (b) for circular CFDSAT sections. The symbol β represents the ratio of B_o/t_o for square sections and D_o/t_o for circular sections and ε denotes the material factor, which is taken equal to $\sqrt{250/f_{0.2}}$ for aluminium alloy, according to EC9 [43]. From Fig. 22(a) and (b), a decreasing trend of normalised flexural strength M_u/M_{pl} can be observed with the increase of the cross-section slenderness parameter for both square and circular specimens. The horizontal line of $M_u/M_{pl} = 1$ separates the cross-sections that have flexural strength equal to or greater than their plastic flexural strength (i.e., $M_u/M_{pl} \geq 1$) from the cross-sections having lower flexural strength than their plastic flexural strength (i.e., $M_u/M_{pl} < 1$). On the basis of this demarcation, it can be seen that the proposed vertical limit lines of 48 and 94 for square and circular CFDSAT cross-sections respectively, separate the sections with normalised flexural strength larger or smaller than unity. Thus, based on the test and FE results of this study, the cross-section slenderness limits of $\beta/\varepsilon = 48$ and $\beta/\varepsilon^2 = 94$ are suggested for square and circular CFDSAT cross-sections.

6. Conclusions

This study experimentally and numerically investigated the behaviour of CFDSAT beams under in-plane bending. Total 10 specimens were tested and 94 specimens were modelled considering different

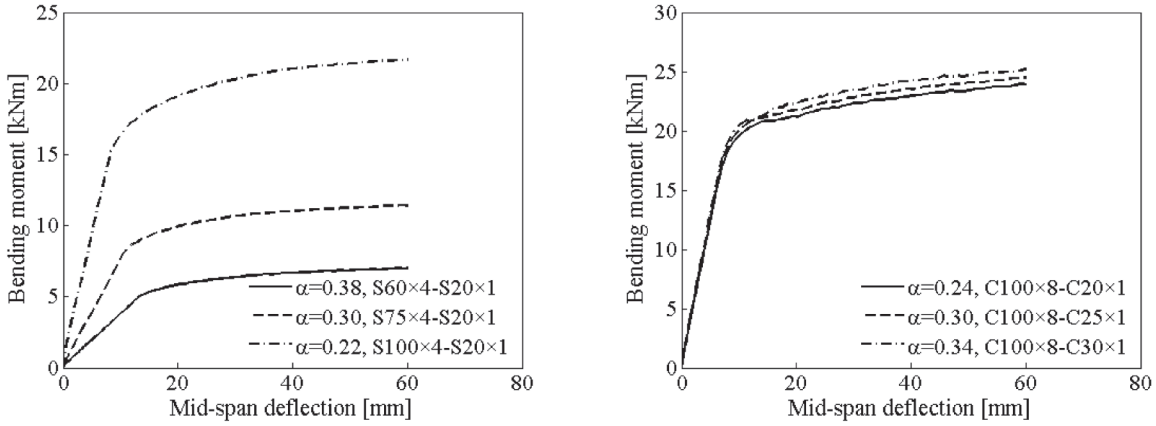

(a) Square CFDSAT specimens - constant inner tube (S20×1)

(b) Circular CFDSAT specimens - constant outer tube (C100×8)

Fig. 13. Effect of hollow ratio on bending moment-midspan deflection curves of typical CFDSAT specimens.

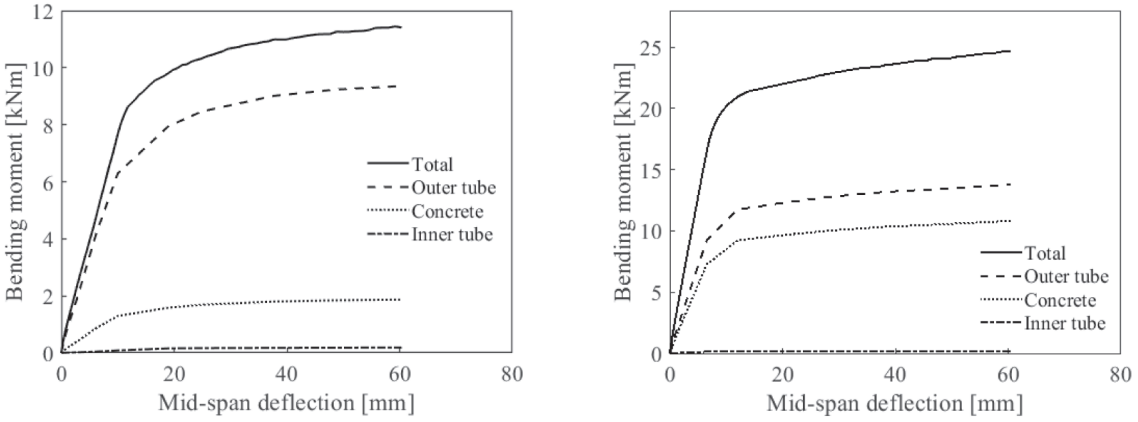

(a) S75×4-S20×1

(b) C100×8-C20×1

Fig. 14. Moment contribution of outer tube, concrete infill and inner tube of typical CFDSAT specimens.

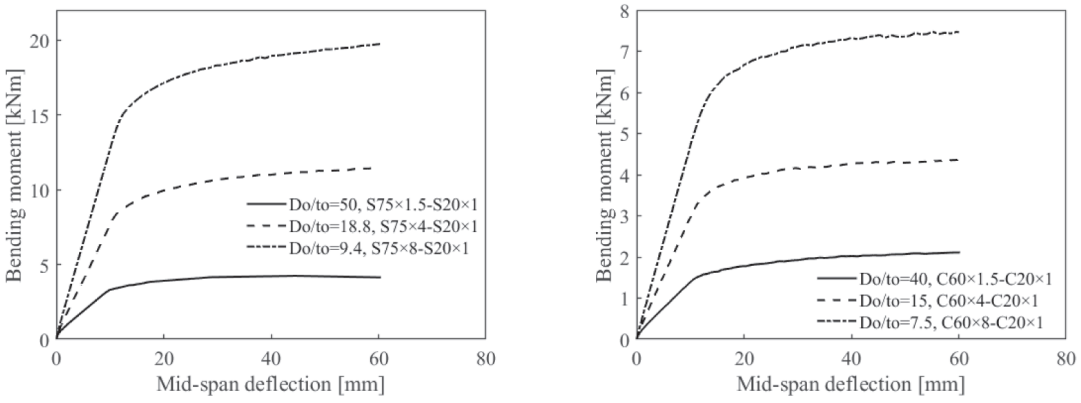

(a) Square CFDSAT specimens

(b) Circular CFDSAT specimens

Fig. 15. Effect of D_o/t_o ratio on bending moment-midspan deflection curves of typical CFDSAT specimens.

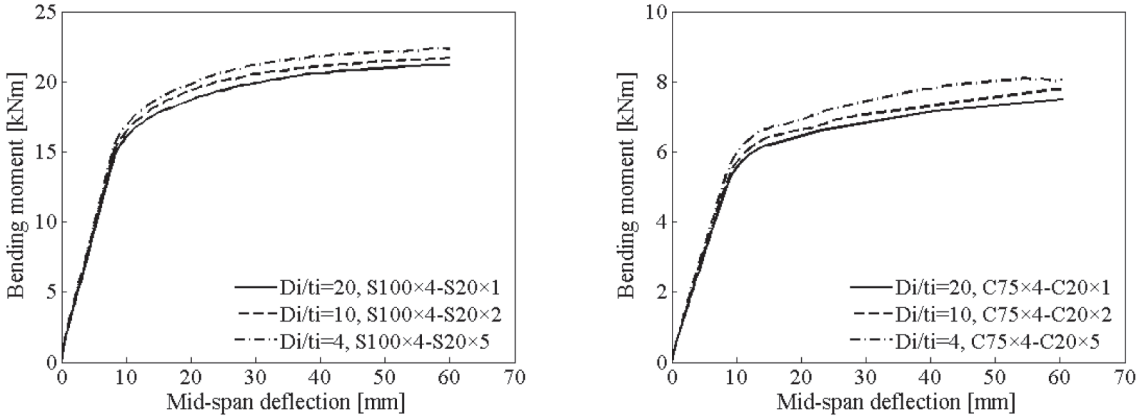

(a) Square CFDSAT specimens (b) Circular CFDSAT specimens

Fig. 16. Effect of D_i/t_i ratio on bending moment-midspan deflection curves of typical specimens.

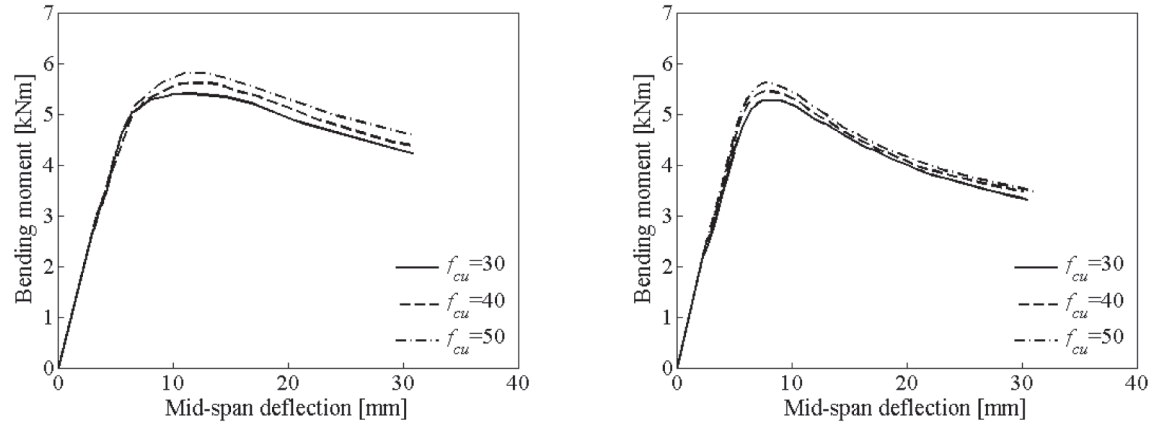

(a) Square CFDSAT specimens (S120×1-C20×1) (b) Circular CFDSAT specimens (C120×1-S20×1)

Fig. 17. Effect of concrete cube compressive strength on bending moment-midspan deflection curves of typical specimens.

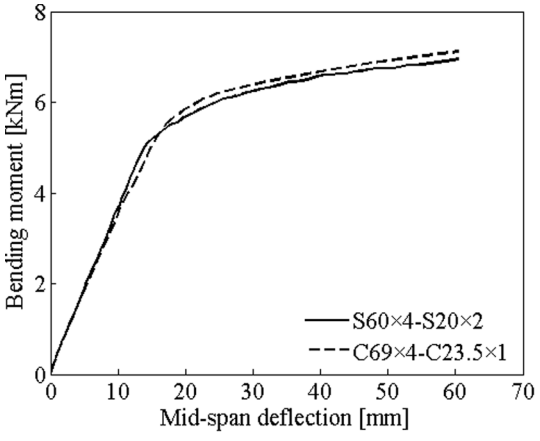

Fig. 18. Effect of cross-section shape on bending moment-midspan deflection curves of typical specimens.

combinations of outer and inner cross-section shapes, i.e., square-square, square-circular, circular-circular and circular-square, over a range of cross-section slenderness and three different concrete cube compressive strengths. The following points can be concluded based on the observed results:

1) The predominant failure mode of all CFDSAT specimens was yielding. Besides yielding, some circular specimens experienced small outward local buckling at the top face of the outer tube and others presented fracture of the outer tube at the tension side upon reaching their flexural capacity. Overall, the concrete infill efficiently prevented the formation of inward local buckling and delayed the occurrence of outward local buckling of the outer tube.
2) The experimental bending moment versus mid-span deflection curves demonstrated that all CFDSAT specimens achieved good ductility, which is attributed to the beneficial composite action of three components of the CFDSAT sections.
3) The developed FE model accurately captured the structural response of the CFDSAT beams. Based on this model a FE parametric study including 94 specimens, was conducted to study the effect of hollow ratio, cross-section slenderness of outer and inner tubes, concrete strength, cross-section shape and composite action on the flexural behaviour of CFDSAT specimens.

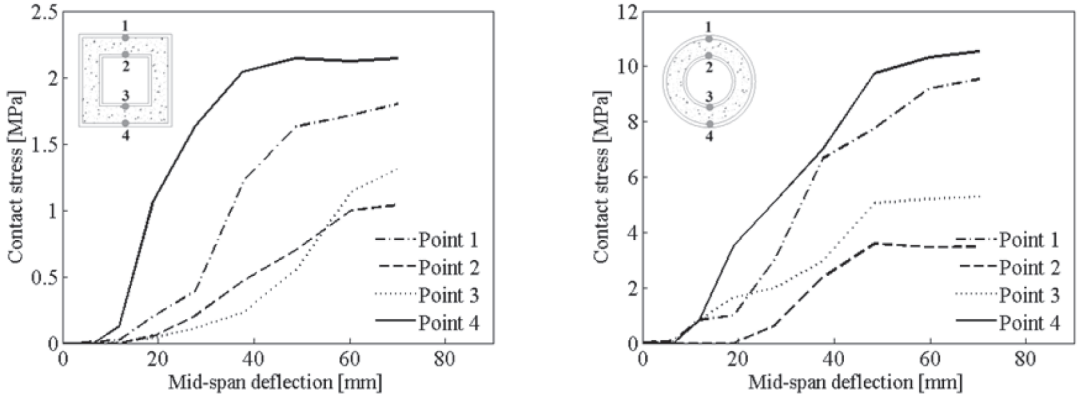

Fig. 19. Contact stresses at mid-span cross-section of typical specimens.

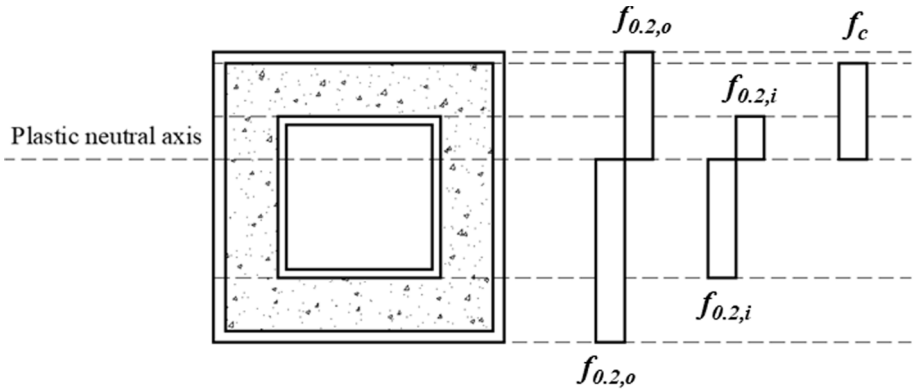

Fig. 20. Plastic stress distribution of a CFDSAT section.

Table 6
Comparison of the design strength with the corresponding test and FE flexural strength.

	Specimen	No	Class of outer section	Class of inner section	$M_u/M_{u,prop}$	
Test	S76.2 × 6.4-S19.2 × 1.6	1	1	1	1.13	
	S76.2 × 6.4-S25.4 × 3.2	1	1	1	1.16	
	S76.2 × 4.8-S25.4 × 3.2	1	1	1	1.19	
	S76.2 × 6.4-C25.4 × 3.2	1	1	1	1.17	
	S76.2 × 6.4-C38.2 × 1.6	1	1	1	1.16	
	C88.6 × 1.6-C19.2 × 3.2	1	4	1	1.03	
	C88.6 × 1.6-C25.4 × 3.2	1	4	1	1.02	
	C88.6 × 1.6-C38.2 × 1.6	1	4	1	1.02	
	C76.2 × 3.2-C25.4 × 3.2	1	1	1	1.18	
	C76.2 × 3.2-C38.2 × 1.6	1	1	1	1.15	
	FE	94	1–4	1–2	1.04	(Mean)
				Mean (all)	1.05	
				COV (all)	0.08	

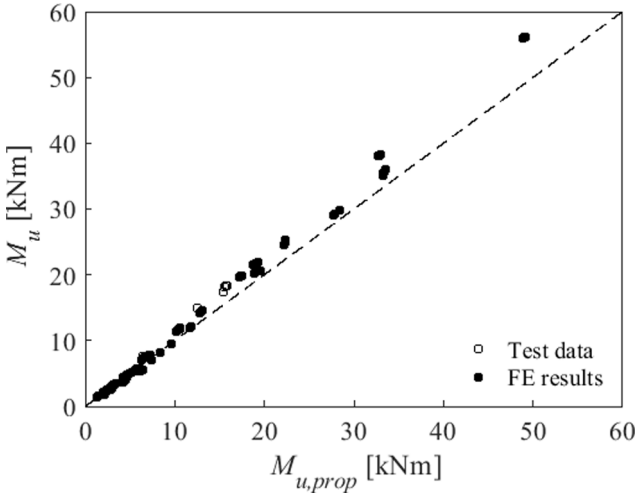

Fig. 21. Comparison of the design flexural strength with the corresponding test and FE flexural strength.

4) The parametric study results showed that the cross-sectional dimensions of the outer tube have a substantial effect on the flexural response of CFDSAT specimens. It was demonstrated that the larger cross-sectional dimensions of the outer tube remarkably increased the flexural strength of the beams.

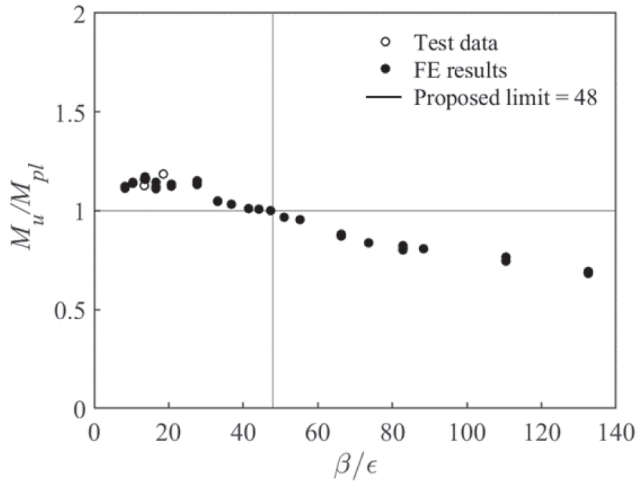

(a) Square CFDSAT specimens

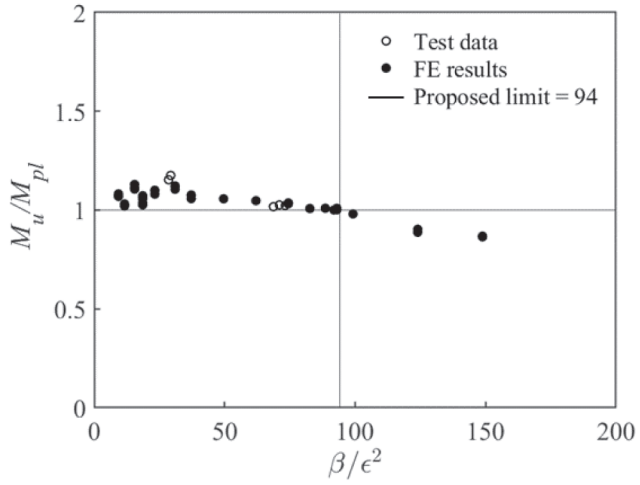

(b) Circular CFDSAT specimens

Fig. 22. Proposed slenderness limits for CFDSAT cross-sections.

5) The flexural strength of CFDSAT beams generally improved with the increase of dimensions of the inner tube and the concrete compressive strength, however, the improvement is less significant.
6) In the absence of design rules, a design methodology is proposed to determine the flexural strength of square and circular CFDSAT beams based on the EC4 framework. It was demonstrated that the proposed methodology accurately predicted the flexural strength of these composite members.
7) Cross-section slenderness limits of $\beta/\varepsilon = 48$ and $\beta/\varepsilon^2 = 94$ for square and circular CFDSAT cross-sections are proposed based on the data obtained from the experiments and FE analyses.

CRediT authorship contribution statement

Shafayat Bin Ali: Conceptualization, Methodology, Software, Validation, Formal analysis, Data curation, Investigation, Visualization, Writing – original draft. **George S. Kamaris:** Conceptualization, Supervision, Writing – review & editing, Funding acquisition, Project administration. **Michaela Gkantou:** Conceptualization, Supervision, Writing – review & editing, Funding acquisition.

Declaration of Competing Interest

The authors declare that they have no known competing financial interests or personal relationships that could have appeared to influence the work reported in this paper.

Data availability

No data was used for the research described in the article.

Acknowledgements

The authors are thankful to the technicians of the Schools of Civil Engineering and Built Environment and Engineering at Liverpool John Moores University for their invaluable assistance. The financial support of the Faculty of Engineering and Technology of Liverpool John Moores University is gratefully acknowledged.

References

[1] Wang F, Young B, Gardner L. Testing and numerical modelling of circular CFDST cross-sections with stainless steel outer tubes in bending. Eng Struct 2021;247:113170. https://doi.org/10.1016/j.engstruct.2021.113170.
[2] Alqawzai S, Chen K, Shen Le, Ding M, Yang Bo, Elchalakani M. Behavior of octagonal concrete-filled double-skin steel tube stub columns under axial compression. J Constr Steel Res 2020;170:106115. https://doi.org/10.1016/j.jcsr.2020.106115.
[3] Li W, Ren Q-X, Han L-H, Zhao X-L. Behaviour of tapered concrete-filled double skin steel tubular (CFDST) stub columns. Thin-Walled Struct 2012;57:37–48.
[4] Mazzolani FM. Aluminium alloy structures. 2nd ed. London: Chapman Hall; 1995.
[5] Mazzolani FM. Competing issues for aluminium alloys in structural engineering. Prog Struct Eng Mater 2004;6(4):185–96.
[6] Georgantzia E, Gkantou M, Kamaris GS. Aluminium alloys as structural material: A review of research. Eng Struct 2021;227:111372. https://doi.org/10.1016/j.engstruct.2020.111372.
[7] Georgantzia E, Ali SB, Gkantou M, Kamaris GS, Kansara KD, Atherton W. Flexural buckling performance of concrete-filled aluminium alloy tubular columns. Eng Struct 2021;242:112546. https://doi.org/10.1016/j.engstruct.2021.112546.
[8] Ali SB, Kamaris GS, Gkantou M, Kansara K, Hashim K. Numerical study of concrete-filled aluminium alloy tubular columns under eccentric compression. IOP Conf Ser: Mater Sci Eng 2021;1058(1):012010. https://doi.org/10.1088/1757-899X/1058/1/012010.
[9] Ali SB, Kamaris GS, Gkantou M, Kansara KD. Concrete-filled and bare 6082–T6 aluminium alloy tubes under in-plane bending: Experiments, finite element analysis and design recommendations. Thin-Walled Struct 2022;172:108907. https://doi.org/10.1016/j.tws.2022.108907.
[10] Chen Y, Feng R, Gong W. Flexural behavior of concrete-filled aluminum alloy circular hollow section tubes. Construct Build Mater 2018;165:173–86.
[11] Chen Y, Feng R, Xu J. Flexural behaviour of CFRP strengthened concrete-filled aluminium alloy CHS tubes. Construct Build Mater 2017;142:295–319.
[12] Zhao X-L, Grzebieta R. Strength and ductility of concrete-filled double skin (SHS inner and SHS outer) tubes. Thin-Walled Struct 2002;40(2):199–213.
[13] Tao Z, Han L-H. Behaviour of concrete-filled double skin rectangular steel tubular beam–columns. J Constr Steel Res 2006;62(7):631–46.
[14] Tao Z, Han L-H, Zhao X-L. Behaviour of concrete-filled double skin (CHS inner and CHS outer) steel tubular stub columns and beam-columns. J Constr Steel Res 2004;60(8):1129–58.
[15] Uenaka K, Kitoh H, Sonoda K. Concrete filled double skin circular stub columns under compression. Thin-Walled Struct 2010;48(1):19–24.
[16] Yan X-F, Zhao Y-G. Compressive strength of axially loaded circular concrete-filled double-skin steel tubular short columns. J Constr Steel Res 2020;170:106114. https://doi.org/10.1016/j.jcsr.2020.106114.
[17] Elchalakani M, Zhao X-L, Grzebieta R. Tests on concrete filled double-skin (CHS outer and SHS inner) composite short columns under axial compression. Thin-Walled Struct 2002;40(5):415–41.
[18] Han L-H, Tao Z, Huang H, Zhao X-L. Concrete-filled double skin (SHS outer and CHS inner) steel tubular beam-columns. Thin-Walled Struct 2004;42(9):1329–55.
[19] Wang F, Young B, Gardner L. Experimental study of square and rectangular CFDST sections with stainless steel outer tubes under axial compression. J Struct Eng 2019;145(11):04019139.
[20] Wang F, Young B, Gardner L. Compressive testing and numerical modelling of concrete-filled double skin CHS with austenitic stainless steel outer tubes. Thin-Walled Struct 2019;141:345–59.
[21] Wang F, Young B, Gardner L. CFDST sections with square stainless steel outer tubes under axial compression: experimental investigation, numerical modelling and design. Eng Struct 2020;207:110189. https://doi.org/10.1016/j.engstruct.2020.110189.
[22] Han L-H, Ren Q-X, Li W. Tests on stub stainless steel–concrete–carbon steel double skin tubular (DST) columns. J Constr Steel Res 2011;67(3):437–52.

[23] Zhao X-L, Tong L-W, Wang X-Y. CFDST stub columns subjected to large deformation axial loading. Eng Struct 2010;32(3):692–703.
[24] Han L-H, Li Y-J, Liao F-Y. Concrete-filled double skin steel tubular (CFDST) columns subjected to long-term sustained loading. Thin-Walled Struct 2011;49 (12):1534–43.
[25] Zheng Y, He C, Zheng L. Experimental and numerical investigation of circular double-tube concrete-filled stainless steel tubular columns under cyclic loading. Thin-Walled Struct 2018;132:151–66.
[26] Hassanein MF, Kharoob OF. Analysis of circular concrete-filled double skin tubular slender columns with external stainless steel tubes. Thin-Walled Struct 2014;79: 23–37.
[27] Sulthana UM, Jayachandran SA. Axial compression behaviour of long concrete filled double skinned steel tubular columns. Struct 2017;9:157–64.
[28] Zhao H, Wang R, Lam D, Hou C-C, Zhang R. Behaviours of circular CFDST with stainless steel external tube: Slender columns and beams. Thin-Walled Struct 2021; 158:107172. https://doi.org/10.1016/j.tws.2020.107172.
[29] Ahmed M, Liang QQ, Hamoda A, Arashpour M. Behavior and design of thin-walled double-skin concrete-filled rectangular steel tubular short and slender columns with external stainless-steel tube incorporating local buckling effects. Thin-Walled Struct 2022;170:108552. https://doi.org/10.1016/j.tws.2021.108552.
[30] Uenaka K, Kitoh H, Sonoda K. Concrete filled double skin tubular members subjected to bending. Steel Compos Struct 2008;8(4):297–312.
[31] Xiong M-X, Xiong D-X, Liew JYR. Flexural performance of concrete filled tubes with high tensile steel and ultra-high strength concrete. J Constr Steel Res 2017; 132:191–202.
[32] Eom S-S, Vu Q-V, Choi J-H, Park H-H, Kim S-E. Flexural behavior of concrete-filled double skin steel tubes with a joint. J Constr Steel Res 2019;155:260–72.
[33] Viet VQ, Ha H, Hoan PT. Evaluation of ultimate bending moment of circular concrete–filled double skin steel tubes using finite element analysis. J Sci Technol Civil Eng 2019;13(1):21–32.
[34] Chen J, Wang J, Xie F, Jin W-L. Behavior of thin-walled dodecagonal section double skin concrete-filled steel tubes under bending. Thin-Walled Struct 2016;98: 293–300.
[35] Zhou F, Young B. Concrete-filled double-skin aluminum circular hollow section stub columns. Thin-Walled Struct 2018;133:141–52.
[36] Zhou F, Young B. Compressive strengths of concrete-filled double-skin (circular hollow section outer and square hollow section inner) aluminium tubular sections. Adv Struct Eng 2019;22(11):2418–34.
[37] Patel VI, Liang QQ, Hadi MNS. Numerical study of circular double-skin concrete-filled aluminum tubular stub columns. Eng Struct 2019;197:109418. https://doi.org/10.1016/j.engstruct.2019.109418.
[38] Kissell J, Ferry R. Aluminum structures: a guide to their specifications and design. New York: John Wiley Sons; 2002.
[39] BS EN 1994-1-1. Eurocode 4 (EC4): Design of composite steel and concrete structures. Part 1-1: General rules and rules for buildings. European Committee for Standardization (CEN), Brussels, 2004.
[40] BS EN ISO 6892-1. Metallic Materials – Tensile Testing – Part 1: Method of test at room temperature. European Committee for Standardization (CEN), Brussels, 2009.
[41] Ramberg W., Osgood W.R. Description of stress-strain curves by three parameters. Technical Note No. 902. Washington, D.C., USA: National Advisory Committee for Aeronautics, 1943.
[42] Hill H.N. Determination of stress-strain relations from “offset” yield strength values. Technical Note No. 927; 1944.
[43] BS EN 1999-1-1. Eurocode 9 (EC9): Design of aluminium structures. Part 1-1: General structural rules - General structural rules and rules for buildings. European Committee for Standardization (CEN), Brussels, 2007.
[44] BS EN 12390-3. Testing hardened concrete. Compressive strength of test specimens. European Committee for Standardization (CEN), Brussels, 2009.
[45] Xu C, Haixiao L, Chengkui H. Experimental study on shear resistance of self-stressing concrete filled circular steel tubes. J Constr Steel Res 2009;65(4):801–7.
[46] Karlsson Hibbitt, Sorensen, Inc. ABAQUS. ABAQUS/Standard User’s Manual Volumes I-III and ABAQUS CAE Manual, 2016. Pawtucket (USA), Version 2016.
[47] Wang J, Afshan S, Gkantou M, Theofanous M, Baniotopoulos C, Gardner L. Flexural behaviour of hot-finished high strength steel square and rectangular hollow sections. J Constr Steel Res 2016;121:97–109.
[48] Gkantou M, Kokosis G, Theofanous M, Dirar S. Plastic design of stainless steel continuous beams. J Constr Steel Res 2019;152:68–80.
[49] Gkantou M, Theofanous M, Wang J, Baniotopoulos C, Gardner L. Behaviour and design of high-strength steel cross-sections under combined loading. Proc Institution Civ Engineers-Struct Build 2017;170(11):841–54.
[50] Tziavos NI, Gkantou M, Theofanous M, Dirar S, Baniotopoulos C. Behaviour of grout-filled double-skin tubular steel stub-columns: Numerical modelling and design considerations. Structures 2020;27:1623–36.
[51] Gkantou M, Theofanous M, Baniotopoulos C. A numerical study of prestressed high strength steel tubular members. Front Struct Civ Eng 2020;14(1):10–22.
[52] Tao Z, Wang Z-B, Yu Q. Finite element modelling of concrete-filled steel stub columns under axial compression. J Constr Steel Res 2013;89:121–31.
[53] Yu T, Teng JG, Wong YL, Dong SL. Finite element modeling of confined concrete-I: Drucker-Prager type plasticity model. Eng Struct 2010;32(3):665–79.
[54] Papanikolaou VK, Kappos AJ. Confinement-sensitive plasticity constitutive model for concrete in triaxial compression. Int J of Solids Struct 2007;44(21):7021–48.
[55] Huang H, Han LH, Tao Z, Zhao XL. Analytical behaviour of concrete-filled double skin steel tubular (CFDST) stub columns. J Constr Steel Res 2010;66(4):542–55.
[56] Wang F, Youn B, Gardner L. Compressive behaviour and design of CFDST cross-sections with stainless steel outer tubes. J Constr Steel Res 2020;170:105942.
[57] Hordijk D. Local approach to fatigue of concrete (PhD Thesis) (Delft: Delft University of Technology). 1991.
[58] FIP. Ceb-Fip Model Code 1990. Ceb-Fip Model Code 1990. 1993.
[59] Bažant Z, Becq-Giraudon E. Statistical prediction of fracture parameters of concrete and implications for choice of testing standard. Cem Concr Res 2002;32:529–56.